UNIVERSITY OF CALIFORNIA SAN DIEGO

Investigations into Electromagnetic Signaling in Cells

A dissertation submitted in partial satisfaction of the
requirements for the degree
Doctor of Philosophy

in

Electrical Engineering (Medical Devices and Systems)

by

Kyle Andrew Thackston

Committee in charge:

        Professor Daniel Sievenpiper, Chair
        Professor Shadi Dayeh
        Professor Dimitri Deheyn
        Professor Eric Fullerton
        Professor Gürol Süel

2020

The dissertation of Kyle Andrew Thackston is approved, and

it is acceptable in quality and form for publication on micro-

film and electronically:

_____

_____

_____

_____

Chair

University of California San Diego

2020

DEDICATION

To John Michael Thackston

EPIGRAPH

You can just quote me.

—Austin Kenny, on what quote I should use

TABLE OF CONTENTS

LIST OF FIGURES

LIST OF TABLES

ACKNOWLEDGEMENTS

022410. 2019. The dissertation author was the primary author of this material.

Chapter 4 is based on "Modeling Electrodynamic Interactions in Brownian Dynamics Simulations" by KA Thackston, M. Casebeer, DD Deheyn, DF Sievenpiper. *In preparation.* The dissertation author was the primary author of this material.

Chapter 5 uses material from "Evidence of intercellular electromagnetic communication in murine embryonic fibroblast culture" by BK Hsiung, KA Thackston, DF Sievenpiper, DD Deheyn. *In preparation.* All material is used with permission by the other authors. The dissertation author was the primary author of this material.

VITA

2015	B. S. in Biomedical Engineering, Purdue University
2016	M. S. in Biomedical Engineering, Purdue University
2020	Ph. D. in Electrical Engineering (Medical Devices and Systems), University of California San Diego

PUBLICATIONS

K.A. Thackston, D.D. Deheyn, D.F. Sievenpiper, "Limitations on electromagnetic communication by vibrational resonances in biological systems", *Physical Review E 101* (6), 062401, 2020

K.A. Thackston, D.D. Deheyn, D.F. Sievenpiper, "Simulation of electric fields generated from microtubule vibrations", *Physical Review E*, 100 (2), 022410. 2019

K.A. Thackston, D.F. Sievenpiper, "Limits of Near-Field Directivity for a Wire Array", *IEEE Magnetics Letters*, 9, 1-4. 2018

K.A. Thackston, H. Mei, P.P. Irazoqui, "Coupling matrix synthesis and impedance-matching optimization method for magnetic resonance coupling systems", *IEEE Transactions on Microwave Theory and Techniques*, 66 (3), 1536-1542. 2017

H. Mei, K.A. Thackston, R.A. Bercich, J.G.R. Jefferys, P.P. Irazoqui, "Cavity resonator wireless power transfer system for freely moving animal experiments", *IEEE Transactions on Biomedical Engineering* 64 (4), 775-785. 2016

ABSTRACT OF THE DISSERTATION

Investigations into Electromagnetic Signaling in Cells

by

Kyle Andrew Thackston

Doctor of Philosophy in Electrical Engineering (Medical Devices and Systems)

University of California San Diego, 2020

Professor Daniel Sievenpiper, Chair

There has long been speculation of inter-cellular communication through weak electromagnetic (EM) fields playing a functional role in biological systems. The predominant theory for how a cell could ever generate electric fields is mechanical vibration of charged or polar biomolecules such as cell membranes or microtubules. The challenge to this theory is explaining how high-frequency vibrations would not be over-damped by surrounding biological media. As many of these suspected resonators are too large for atomistic molecular dynamics simulations, accurately modeling biological resonators remains an ongoing challenge. Starting with energy transfer expressions from coupled-mode theory, we derive expressions for the minimum quality factor required to sustain communication for both near- and far-field interactions. Next, we ana-

lyze microtubules as candidate "antennas", using a custom electromagnetic simulation technique to assess the field strength from vibrating microtubules. Building off the difficulties of simulating the microtubule in conventional molecular simulation techniques, we develop our own method of simulating electrodynamic interactions in biological systems and implement it for a model of linear DNA. Lastly, we discuss experimental work with our collaborators in the biological sciences. We developed a series of band pass filter frequency selective surfaces to narrow down the frequency of signaling in barrier experiments, then followed up with listening and stimulation type experiments in the biologically active frequency spectrum. Overall, our modeling suggests that any potential biological EM signaling could not overcome the damping from surrounding viscous media, at least based on identified biological resonances. Biological resonators contain insufficient charge or dipole moments to produce significant fields to overcome background thermal energy. Electrodynamic interactions seem to require electric fields or velocities unrealistic in biological systems. Our experimental results are mixed in their findings, giving indirect evidence of biological signaling, but providing no direct measurement of EM signals.

Chapter 1

Introduction

Biological signaling is necessary for the orchestration of various processes of life. Most biological signaling is chemical. Cells release chemicals which transport diffusively and are detected by other cells, triggering some appropriate response. In complicated multi-cellular organisms, nerve cells conduct signals quickly over large distances electro-chemically. Some cells are also mechanically sensitive, making mechanical signaling sometimes viable.

It has been speculated that electromagnetic (EM) fields may be an undiscovered modality of biological signaling [1]. This field has a complex history which I will attempt to summarize in this introduction. The literature is controversial and somewhat lacking in authoritative reviews. Our study was conducted as part of the DARPA RadioBio grant, which sought to investigate the possibility of purposeful EM communication in biological systems.

First I will give a brief history of EM theories of biological signaling. Next I will clarify exactly what we mean by EM signaling, ruling out other similar areas of study such as thermal exposure or conductive signaling. Finally I will outline the remainder of this thesis and how we attempted to answer these questions through mathematical modeling and experiment.

1.1 A History of Biological Radios

I will attempt to provide historical context of biological EM signaling, because I believe the topic to be a particularly non-traditional problem. There is indeed a great deal of literature on the subject. Some of these studies are robust, many of them are controversial, and some of them are plain pseudo-science. I believe honest study of this subject cannot occur without confronting its controversial history. Before beginning, it is helpful to review the symptoms of pseudoscience to review the following material with a critical eye [2]:

1. **Vague, exaggerated or untestable claims**: Many of these works make exceedingly grand claims, asserting that fringe theories are "well known" and that pure conjectures are "accepted". They draw dramatic conclusions from weak evidence.

2. **Over-reliance on confirmation rather than refutation**: This is perhaps the most popular trend. Many of these works rely on a reverse burden of proof, make hypotheses that are not falsifiable, and suppress or ignore studies in conflict with their own.

3. **Lack of openness to testing by other experts**: This is typically manifested by casting doubt on negative experiments. Supporters will discount negative replications, claiming that many seemingly non-relevant factors were not controlled for, such as the time of year, location of the lab, and weather conditions [1].

4. **Absence of progress**: While there are many areas that have progressed significantly, there are some (such as barrier experiments) that have remained stagnant for nearly a century.

5. **Personalization of issues**: This is less common, and typically only prevalent among the most obvious of charlatans.

6. **Use of misleading language**: Many math and physics terms are used loosely, seemingly to obfuscate and discourage refutation. I have found the most commonly abused terms are "resonance", and "quantum", "fractal" [3, 4].

1.1.1 Mitogenetic Radiation

In the 1920s, Russian biologist Alexander Gurwitsch had been developing the concept of the "morphogenic field" to answer some questions in embryology, concerning how cells differentiate. The morphogenic field was intended to be some sort of life force that would tell cells what to do. While this may seem primitive in retrospect, one must remember this was decades before the discovery of DNA.

In 1923, Gurwitsch performed an experiment in which he separated onion roots with various barriers and observed how quickly they grew. He determined that the onions grew faster when separated with quartz barriers, but not glass barriers. Because glass blocks UV and quartz does not, he inferred there was some UV signal being emitted by the onions as they grew that encouraged further growth. He called this "mitogenetic radiation". This exerpimental setup, known as a "barrier experiment", and has continued even in modern times, nearly a century later [5, 6].

Interactions between radiation and biology was already a trendy topic at the time. By the early 1930s, there were nearly 600 papers and books on mitogenetic radiation [7]. People suddenly were claiming evidence of mitogenetic radiation not just from onions, a variety of organic and even inorganic sources. There were many labs, particularly in the West, who found themselves unable to reproduce any of Gurwitsch's results [8]. The controversy grew so extensive that in 1935, the US National Research Council set aside a grant to generate conclusive evidence on the existence of mitogenetic radiation. The study was unable to detect any evidence of the controversial radiation [7]. Publications on the subject nearly ceased entirely. For some, the entire subject of mitogenetic radiation has become a canonical example of "pathological science" [9].

But this did not discourage Gurwitsch, who along with his wife / collaborator Lydia continued to push the theory of mitogenetic radiation. After concepts like DNA and chromosomes became more mainstream in the 40s and 50s, the morphogenic field theory lost any remaining steam and even Gurwitsch later adjusted the theory in light of new evidence. In 1941, he was

even awarded the Stalin Prize for his work on mitogenetic radiation and claims that this was a cheap method of diagnosing cancer. With the rise of Trofim Lysenko, Gurtwitsch chose to retire from his university position. He continued to work from home until his death in 1954. Anna Gurwitsch, Alexander's daughter, continued his research and advocated for mitogenetic radiation [10]. Theories on mitogenetic radiation continued to be popular in the USSR and Russia, branching off into studies on cellular emissions from the UV to infrared to microwave frequencies [1].

1.1.2 Biophotons

German biophysicist Fritz Popp coined the term "biophoton" term in the 1970s after directly measuring photons emitted from biological systems above thermal levels [11, 12]. Supporters of Gurwitsch's theory claim that this finally proved the existence of mitogenetic radiation, but there is not clear evidence linking the emissions observed by Popp to the increased rate of mitosis observed by Gurwitsch. Though the existence of biophotons is not heavily disputed, it is not widely believed they serve any biological function. The most popular hypothesis is that spontaneous biophotons are emitted from chemical reactions in cells, often involving free radicals [13]. In this theory, biophotons are more like traffic noise emitted from a bustling cell, rather than an intentional mechanism of communication. While biophotons fall under basic science research, there is hope that a better understanding could have applications for diagnostic applications.

And unfortunate offshoot of this research has been "biophoton therapy", which maintains that special UV exposure can be used to treat various health conditions. Many in the medical community have been quick to dispute these claims. Popp himself has argued against the quantum health clinics [14].

There has also been discussion of biophotons being used for purposeful cellular signaling [15, 16]. In general the evidence is not overwhelming, though this could be attributed to the difficulties and inconsistencies associated with biophoton measurement across across different

laboratory environments.

1.1.3 Fröhlich Condensates

Independent of the theory of biophotons and mitogenetic radiation, the British-German physicist Herbert Fröhlich published his firs work relating to biology in 1968 on the theory of a "Fröhlich condensate". Fröhlich theorized that collections of electrically polar proteins could exhibit coherent vibrations. He suggested that the collection of resonators could condense and display macroscopic quantum coherence, in a manner similar to Bose–Einstein condensation but at room temperatures [17, 18, 19]. Fröhlich predicted energy from other parts of the cell condensing and leading to emissions on the order of 100 GHz. In the 1970s, Fröhlich was further encouraged by studies he found in the USSR claiming to measure 100 GHz emissions from yeast cells.

In 2009, a computational study of Fröhlich condensates concluded such condensates are "inaccessible in a biological environment" [20]. In 2015, a different group of scientists claimed to measure a Fröhlich condensate by exposing an egg white with a weak excitation of 400 GHz radiation [21], though there was no consensus on whether this constituted a true condensate or not [22]. There does not appear to be an overwhelming consensus on the proper definition of a Fröhlich condensate.

Overall some works will invoke the concept of the Fröhlich condensate, or other quantum mechanical phenomena, to justify theories which seem falsified by classical physics. There is particular interest, as will be seen the following section, of tying Fröhlich condensates to information processing [23, 24].

1.1.4 Orchestrated Objective Reduction

While the subject of consciousness may seem out of the scope of this thesis, one cannot discuss biological EM signaling without stepping into the realm of quantum consciousness theorists. In 1989, the celebrated mathematician Sir Roger Penrose published his first book on consciousness, The Emperor's New Mind. Based on Gödel's theory of computability, Penrose argued that the human brain was able to prove things that were "noncomputable" by a classical computer. This led him to conclude that consciousness must be quantum mechanical in nature [25]. This was basically a theoretical extension of the notions of Gödel and later the philosopher John Lucas, who already had suggested the human brain could not be purely mechanical.

Penrose's book piqued the interest of anesthesiologist Dr. Stuart Hammeroff, who had already been researching the possible role of microtubules in information processing in the brain. Microtubules, as the name implies, are very small tubes, about 23 nm in diameter and up to many microns long. They are also electrically polar, having a positive end and a negative end. The constituent protein of microtubules, tubulin, is known for being particularly electrically polar. Microtubules serve as bones of the cell, as pathways for transport proteins to crawl along, and play an important role in cell division [26].

Hammeroff pitched to Penrose that microtubules were candidates for a Fröhlich condensate, and this could be a way that quantum physics could be entangled with neurons. The idea is that microtubules are very stiff, and could sustain high frequency mechanical vibrations. These vibrations could generate electric fields that might induce vibrations in neighboring microtubules, thus leading to the ensemble of oscillating proteins Fröhlich predicted. This in turn, they suggested, would lead to the quantum information processing necessary for consciousness. The two of them went on to develop this theory in the early 1990s, which they titled Orchestrated Objective Reduction (Orch OR) [27, 28].

The Orch OR hypoethesis has been widely criticized by mathematicians, computer scientists, physicists, neuroscientists, and philosophers [29, 30, 31, 32, 33, 34]. From a mathematical

perspective, critics say that Penrose's argument confounds strict mathematical definitions with looser philosophical ones. Physicists largely agree that the human body is too noisy, warm, and wet to sustain any quantum coherence. And biologists point out that microtubules do not seem to have the critical role near the gap junctions of neurons that Hameroff suggested. Penrose and Hameroff have attempted to counter these criticisms, but their ideas have not gained much ground in the scientific community. They have, however, found success in notorious pseudo-scientific figures such as Depak Chopra, further reducing scientific credibility.

1.2   Scope of this Thesis

In this work we will attempt to objectively evaluate the likelihood of EM signaling in biology. The total scope of possible power and frequency regimes is great. Our goal is to encompass as broad a regime as possible while still being able to make practical claims. We therefore restrict ourselves to the ranges and categories specified below:

- **Frequency**: In this work we study interactions typically in the radio frequency to microwave spectrum, though much of this analysis would be applicable for lower frequencies and up to the terahertz regime. Since we are interested in non-photonic interactions, we do not consider infrared or smaller wavelengths in this work.

- **Power levels**: It is reasonable to assume any EM field generated by a cell would be extremely low power, or else it would likely have been detected by now. We are concerned only with non-thermal, non-ionizing interactions. A good rule of thumb for radiating waves is that thermal interaction starts at $1 \, \mathrm{mW/cm^2}$ [35]. Communication which relies on thermal mechanisms seems unlikely, as such power levels would be difficult to generate.

- **Mechanism**: The main mechanism we consider is generation of EM fields through mechanical vibration of permanent dipole moments. This is different than a traditional antenna

which relies on currents on a conductive body to produce the accelerating charge that results in radiation.

We will not consider photonic or quantum effects in this work. This is not to say that quantum biology has nothing to contribute; there has been significant research suggesting that magneto-reception in birds is quantum mechanical in nature [36]. Since the arguments for quantum coherence in biological systems seem currently weak, we do not account for any entanglement or other quantum effects in our analysis.

Communication that relies on electrical current flow will also be excluded. For example, sharks and other weakly electric fish have a strong sense of electro-reception. In sharks, this comes from specialized organs known as the Ampullae of Lorenzini [37]. Certain species such as elephant fish use this even for electro-location and electro-communication [38]. All of these mechanisms rely on conductive media, such as salt water, to conduct charge injected into the medium.

We also do not focus on large specialized organ systems (i.e. one could argue eyes are allow communication across the visible light spectrum, but this trivial example is not relevant to this work). In a less trivial example, it has also been demonstrated that honey bees can collect static charge from flight and detect the charge on other flowers or bees. This does not use typical electro-reception, but a form of mechano-reception where their antennae are sensitive to static fields [39]. Our work will be limited to length scales smaller than tissue and organ systems, on the length scale of cells and smaller.

In Chapter 2, we will attempt to tackle the question of EM signaling from the top down. Starting with abstract models of biological resonators, we will work to determine under what conditions biological communication can occur. Namely, we will derive the limits on damping imposed by energy transfer constraints. We assume that for communication to occur, interaction energy must exceed background thermal energy. There is no credible hypothesis for how time averaging or other signal processing could occur in sub-cellular processes, so that will not be

8

taken into account. After deriving damping limitations for far and near field cases, we see if any previously modeled biological resonances can meet our criteria. We find that only one microtubule simulation can satisfy our criterion, and only with significant assumptions.

In Chapter 3, we move from an abstract resonator model to a more concrete simulation of a microtubule. We assume the microtubule is undergoing mechanical vibration. Our goal is to determine if the electric fields generated by vibrations would ever be strong enough to influence other biological systems or induce vibrations in neighboring microtubules. We demonstrate the flaws in previous work simulating such fields, and develop our own transient method to simulate microtubules vibrating in a conductive medium.

In Chapter 4, we reflect on the difficulties of simulating the microtubule in Chapter 3, and our inability to simulate the structure in a more conventional simulation technique. Seeking to generalize bio-electrodynamic simulations, we develop a technique that allows one to simulate high frequency or high power stimulations in a Brownian Dynamics simulation. We discuss the regimes where this method would be more appropriate than the electrostatic assumption. To investigate the impact, we develop a simple rod and bead worm-like-chain model of linear DNA, a negatively charged biomolecule, and simulate the impact of the electrodynamic forces under high power pulses.

Finally in Chapter 5, we discuss our experimental efforts to detect evidence of purposeful biological EM signaling. This will primarily involve our work on with barrier experiments, in which we design frequency selective surface (FSS) bandpass filters to serve as various barriers. We follow this up with attempts to detect cellular EM fields directly.

Chapter 2

Limitations on Electromagnetic Signaling using Vibrational Resonances

The most obvious obstacles to purposeful EM signaling is how cells would ever generate an electromagnetic field of sufficient strength such that a neighboring cell could detect it. As discussed in Chapter 1, Herbert Fröhlich theorized that collections of electrically polar proteins could exhibit coherent vibrations. His work even suggested that the vibrating structures could condense and display macroscopic quantum coherence, in a manner similar to Bose–Einstein condensation [17, 18, 19]. No examples of such condensates have been found, and further theoretical research has concluded such condensates are "inaccessible in a biological environment" [20].

Even without the exotic quantum properties predicted by Fröhlich, most hypotheses of cellular EM generation involve some sort of electromechanical coupling. If a cell could somehow deliver energy to charged or polar proteins and induce high frequency mechanical vibrations, the resulting oscillation of charges would produce a time-varying field. Various structures have been investigated as potential EM receivers or transmitters, namely the microtubules of the cytoskeleton [40, 41, 42], cell membranes [43], viruses [44, 45, 46, 47], and DNA [48, 49]. Purely

electromagnetic resonances have also been investigated [50]. In this work we limit ourselves to structures where an electromagnetic field couples into a mechanical mode, since this seems more likely to be deliberately excited by a cell.

Accurately modeling the many hypotheses of electromechanical signaling remains a difficult problem. Fundamentally, however, all these mechanisms can be distilled down to interactions with coupled resonators and electromagnetic fields. Instead of modeling specific mechanisms and evaluating their ability to sustain communication, we seek to abstractly model the problem of coupled resonator communication. In this chapter, we present our unique analysis to impose criterion on EM signaling based on energy constraints.

While defining "purposeful communication" in a physically meaningful way is certainly challenging, in this work, we will consider an interaction significant if it imparts more energy than the background thermal energy. This is a necessary but not sufficient condition for communication to occur. Since most of the proposed hypotheses of biological EM communication are concerned with intra and inter-cellular communication, we focus on structures with length scales ranging from the molecular to the cellular level (up to $10\,\mu\text{m}$). Larger structures such as cell aggregates and tissues will not be considered.

The quality factor (Q factor) of a resonator is a parameter that describes how strongly a resonator's oscillations are damped. We derive expressions for the minimum Q factor required for an oscillator to interact with an incoming plane wave, and for interacting oscillators in each other's near field. We evaluate where past studies fit into our framework and draw conclusions about the likelihood of these structures engaging in electromagnetic communication between or within cells.

2.1 Electric Field Screening in Electrolytic Media

An important barrier to inter-cellular electric field communication is the impact of screening from counter-ions in biological media. Charged or polar molecules attract a counter ion cloud around them, exponentially attenuating electrostatic fields after a few molecular layers. The Debye length characterizes the size of the counter ion cloud, and is about 1 nm for cytosol [51]. For electromagnetic interactions to be considered "long distance", they must occur at length scales larger than the Debye length.

Time varying fields, however, can overcome screening from conductive media if the oscillation rate can exceed the mobility of the counter ions. Because our length scales of interest are much less than relevant skin depths at these frequencies, we can choose to ignore skin depth effects. Conductive media then acts as a high pass filter with a cutoff around the Maxwell, or plasma, frequency, given by $\omega_p = \sigma/\varepsilon$ where σ is the conductivity of the medium and ε is the permittivity [52]. This is often expressed as a complex frequency dependent permittivity given by $\underline{\varepsilon} = \varepsilon - i\sigma/\omega$. Compared to fields in a lossless dielectric, fields are attenuated by a factor of A given by Eq. 2.1 and plotted in Fig. 2.1:

$$A(\omega) = \frac{1/\underline{\varepsilon}}{1/\varepsilon} = \frac{\varepsilon\omega}{\varepsilon\omega - i\sigma} = \frac{1}{1 - i\omega_p/\omega} \tag{2.1}$$

For biological solutions such as cytosol, the conductivity is approximately 1.1 S/m and the relative permittivity is about the same as water, which is approximately 80 [53]. Therefore the Maxwell frequency is approximately 250 MHz, though this will of course vary based on the conductivity of the solution [53].
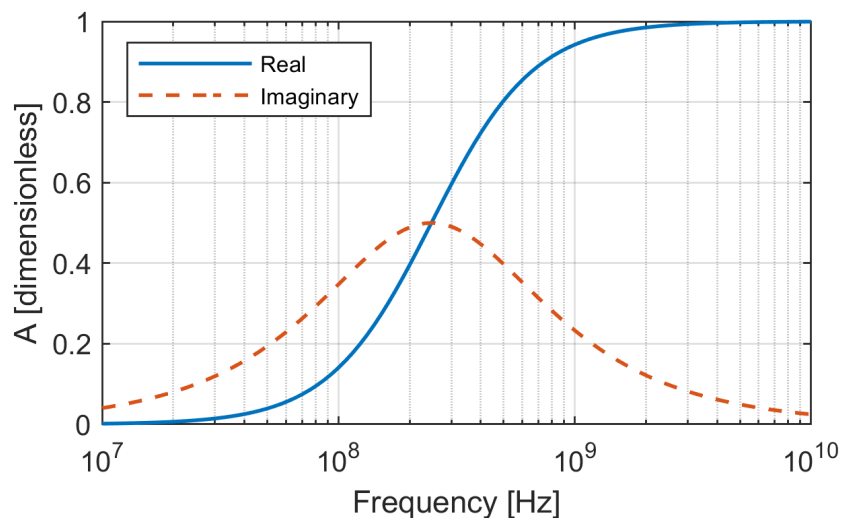
Figure 2.1: Attenuation factor (given by Eq. 2.1) of electric quasi-static electric fields by conductive media when $\varepsilon_r = 80$ and $\sigma = 1.1\,\mathrm{S/m}$.

2.2 Minimum Q Factor for Far Field Interactions

First we examine the possibility of cell-to-cell communication through far field electromagnetic waves. Instead of focusing on how the fields would be generated in the first place, we analyze the case of some resonant dipole protein being hit with an incoming plane wave as depicted in Fig. 2.2a. Our analysis is similar to that of Adair where he explored how low power microwaves might influence biological resonators [54]. Unlike Adair, we model the system as an antenna and use the Wheeler-Chu limit to find a bound on our scattering Q factor, thus allowing us to relate Q factor to the resonator size. We will define a minimum absorption Q factor required for any resonator to absorb significant energy (greater than the background thermal bath) from an incoming plane wave using the absorption cross section given by coupled mode theory.

2.2.1 Energy Absorbed by Resonant Scatterer

We can calculate the power absorbed by the resonator in Fig. 2.2a by defining an absorption cross section. The power absorbed (P_a) by the resonator when hit with an incoming

13
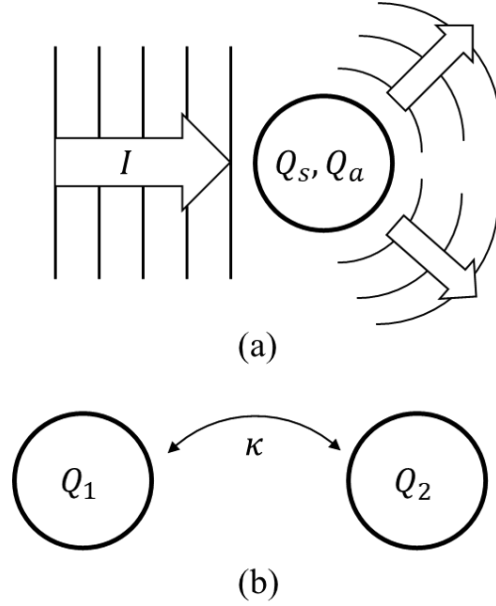
Figure 2.2: Illustration of resonators interacting with electromagnetic fields. (a) Incident field with intensity I scattering off a resonator with scattering (radiative) quality factor Q_s and absorption quality factor Q_a. (b) Two resonators with their own quality factors coupled in the near field with coupling coefficient κ.

plane wave with intensity I is given by

$$P_a = \sigma_a I \tag{2.2}$$

where σ_a is the absorption cross section with units of area. The absorption cross section of a resonant dipole hit with an incident electromagnetic plane wave is given by Eq. 2.3, which is a form of the Breit-Wigner formula and has also been proven for more general cases using coupled mode theory [55, 56].

$$\sigma_a(\omega) = \frac{3\lambda^2}{2\pi} \frac{\Gamma_s \Gamma_a}{(\omega - \omega_0)^2 + \Gamma^2}. \tag{2.3}$$

Here λ is the wavelength, Γ_s is the scattering spectral half width half maximum (units of frequency), Γ_a is the absorption spectral half width half maximum, ω is the angular frequency, ω_0 is the resonant frequency, and the total width $\Gamma = \Gamma_s + \Gamma_a$. The total width is the inverse of the corresponding relaxation time of the resonator ($\Gamma = 1/\tau$). This expression is valid for electrically

small ($\ll \lambda$) resonant dipoles near the resonant frequency.

The total Q factor is defined as the ratio of the peak energy stored in the resonator to the energy lost (absorbed) per cycle. This can also be expressed in terms of the resonant frequency and the relaxation time of the resonator, as shown in Eq. 2.4.

$$Q \equiv \frac{\omega_0 U_{max}}{P_a} = \frac{\omega_0 \tau}{2} \tag{2.4}$$

The maximum energy the resonator can store is therefore:

$$U_{max} = P_a \tau / 2 = \sigma_a I / 2\Gamma. \tag{2.5}$$

The absorption cross section, and therefore the power absorbed, is largest at the resonant frequency.

$$\sigma_a(\omega_0) = \frac{3\lambda^2}{2\pi} \frac{\Gamma_s \Gamma_a}{\Gamma^2}. \tag{2.6}$$

The lowest anticipated frequencies of cell to cell communication are around 100 MHz. At lower frequencies, the electric fields are attenuated by Debye screening as discussed in Section 2.1. This means the smallest wavelength of interest in free space is approximately 3 mm (or about 340 μm in water). As mentioned previously, our length scale of interest in expected biological resonators is at most on the order of 10 μm, therefore we can safely assume the resonator is much smaller than the wavelength. It follows the absorption width is much larger than the scattering width ($\Gamma_a \gg \Gamma_s$). In antenna physics terms, this is the same conclusion one would draw for an electrically small antenna. The resonant cross section can therefore be approximated as

$$\sigma_a(\omega_0) \approx \frac{3\lambda^2}{2\pi} \frac{\Gamma_s}{\Gamma_a}. \tag{2.7}$$

The maximum energy the resonator can store can therefore be approximated as well,

$$U_{max}(\omega_0) = \sigma_a(\omega_0)I/2\Gamma \approx \frac{3I\lambda^2\Gamma_s}{2\pi\Gamma_a^2}. \tag{2.8}$$

In order for an interaction to be considered biologically significant, the resonator must be able to store more than thermal energy (k_BT, where k_B is the Boltzmann constant and T is temperature) from the interaction. For N resonators acting coherently, that restriction may be relaxed to $k_BT/\sqrt{N}$ [54]. By setting Eq. 2.8 equal to this minimum energy, we can solve for the maximum absorption width for which significant interaction could occur.

$$\Gamma_a < \sqrt{\frac{3I\lambda^2\Gamma_s\sqrt{N}}{2\pi k_BT}} \tag{2.9}$$

2.2.2 Limiting the Scattering Width using the Wheeler-Chu Limit

In order to set bounds on Eq. 2.9, we need to set a bound on the scattering width. From Eq. 2.4, we see the resonant widths are related to Q factors by $\Gamma_i = \omega/2Q_i$. The absorption width can be shown to be related to the internal loss of the resonator (energy absorbed by the resonator) and the scattering width is related to the radiative loss of the resonator (energy reflected back into the surroundings).

By analyzing the resonator as a small antenna, we can set bounds on the Q factor based on only frequency and size. The Wheeler-Chu limit sets a lower limit on the scattering Q factor of any small antenna [57].

$$Q_s \geq \frac{1}{k^3a^3} \tag{2.10}$$

where $k = 2\pi/\lambda$ and a is the radius of the smallest sphere enclosing the resonator. The wavelength is given by $\lambda = c_0/f\sqrt{\varepsilon_r}$ where ε_r is the relative permittivity of the medium and c_0 is the speed of light in a vacuum. Achieving the Wheeler-Chu limit is difficult in most small antenna designs, so it is unlikely that a biological resonator would even approach this limit.

2.2.3 Minimum Absorption Q Factor

First, we substitute the widths in Eq. 2.9 with their corresponding Q factors. To assume the best case scenario, we set the scattering Q factor $Q_s = 1/k^3a^3$ from Eq. 2.10. This gives us the following expression for the lower bound of the absorption Q factor required to store more than background thermal energy from an incoming plane wave.

$$Q_a \geq \sqrt{\frac{c_0 k_B T}{6\pi I a^3 \sqrt{\varepsilon_r N}}}. \tag{2.11}$$

Note that Eq. 2.11 is dependent only on temperature, plane wave intensity, the permittivity of the medium, the number of resonators, and the size of the resonator. So long as the resonator is much smaller than the wavelength, the requisite Q_a is independent of frequency.

One upper limit of plane wave intensity can be derived from the power generated by a single cell. From thermodynamic arguments, a single human cell generates on the order of 10^{-12} Watts [58]. If we assume a relatively small cell with a 1 μm radius, we can estimate the maximum possible radiation intensity as $I = P/4\pi r^2$, giving us $0.08\,\text{W/m}^2$, or $8 \times 10^{-3}\,\text{mW/cm}^2$. Note that this is much smaller than the maximum intensity allowed by the FCC for general population EM exposure between 1.5-100 GHz, which is $1\,\text{mW/cm}^2$ [35].

In Fig. 2.3, we plot the minimum Q factor for both of these power intensities as a function of resonator size. We assume that the dielectric of the medium will be similar to water and have a relative permittivity of 80. The temperature will be assumed to be 300 K. We see as the resonator becomes larger, the Q factor required decreases. The requisite Q factor also decreases as the power intensity increases. We also see that increasing the number of coherent resonators can decrease the minimum Q factor, though not dramatically. As suggested by Eq. 2.11, it requires 10,000 coherent resonators to result in a factor of 10 decrease for the minimum Q factor. The Q factors required for sub-cellular resonators (10-100 nm), are quite large (> 100) given the low power intensity. This is consistent with past works which have evaluated far field coupling of
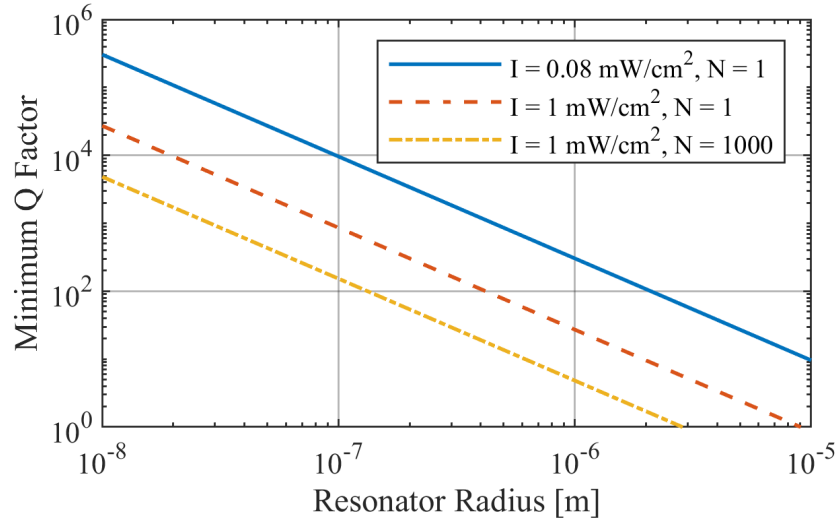
Figure 2.3: Minimum Q factor required for an incoming plane wave of intensity I to impart more energy than $k_B T$ on a dipole resonator. Plotted as a function of the radius of the smallest sphere enclosing the resonator. The temperature is assumed to be 300 K and the relative permittivity of the media is 80 (water).

biological resonators to be insignificant at non-thermal levels [54, 59, 60].

2.3 Minimum Q Factor for Near Field Interactions

We can make similar arguments to construct a minimum Q factor for two resonators with a coupled near field, corresponding to the case in Fig. 2.2b. Energy transfer between coupled resonators can be described by two dimensionless parameters: the Q factor of each resonator and the coupling coefficient (κ) between the resonators. For the remainder of our analysis we will refer to the absorption Q factor Q_a as simply "the Q factor" since the scattering Q_s does not play a role in the near field analysis. The coupling coefficient is a normalized, dimensionless mutual energy metric ranging from zero to one. Strongly interacting resonators will have a coupling coefficient near one, whereas weakly interacting ones will be closer to zero.

Analyzing resonators in terms of Q factors and couplings is used often in microwave filter theory, where the coupling coefficient represents electrical or magnetic coupling between
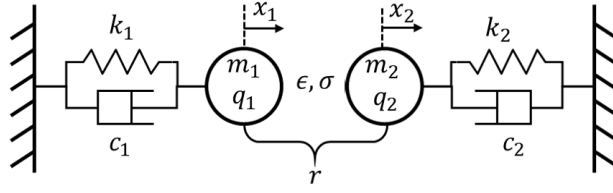
Figure 2.4: Coupled spring mass resonators submerged in fluid. Each resonator has mass m, charge q, spring constant k, and damping coefficient c. The media has permittivity ε and conductivity σ. At rest, both resonators are separated by distance r.

resonators [61]. In this biological context, we are concerned with electrically coupled mechanical resonators. First we will will derive an expression for the coupling coefficient for a simple case of charged mass spring resonator to gain some intuition about the nature of the coupling. Then we will derive the minimum Q factor needed based on the power transfer efficiency between the resonators.

2.3.1 Electrically Coupled Mechanical Resonators

In order to gain insight on the electromechanical coupling coefficient, we analyze the simple case of two coupled mass spring resonators, as depicted in Fig. 2.4. Each mass carries a charge, therefore interaction between resonators occurs via the electric field. The resonators are submerged in a fluid medium resulting in drag for each mass.

Let us define $\Delta x(t) = x_1(t) - x_2(t)$. The force induced on resonator 2 by the electric field generated by resonator 1 is given by:

$$F_{21} = q_2 E_1 = \frac{q_1 q_2}{4\pi \underline{\varepsilon}(r - \Delta x(t))^2} \tag{2.12}$$

Where q_1 and q_2 is the charge of resonator 1 and 2 respectively, r is the distance between the resonators when $\Delta x(t) = 0$, and $\underline{\varepsilon} = \varepsilon - i\sigma/\omega$.

Assuming the amplitude variables are much smaller than the distance between the res-

19

onators ($r \gg \Delta x(t)$), then we can expand Eq. 2.12 using a Taylor series expansion.

$$F_{21} = \frac{q_1 q_2}{4\pi\underline{\varepsilon}r^2} - \frac{2q_1 q_2 \Delta x(t)}{4\pi\underline{\varepsilon}r^3} + O(\Delta x(t)^2) \tag{2.13}$$

We note that the first term is constant over time. This DC offset goes to zero because of Debye screening, as explained in section 2.1. Assuming that the oscillations will be very small, we ignore higher powers of Δx and leave ourselves with the dipole approximation. We see this inter-dipole force is dependent on the position of both resonators much like a spring connecting both masses. We define this inter-resonator mutual spring constant as

$$k_m = \frac{q_1 q_2}{2\pi\underline{\varepsilon}r^3} \tag{2.14}$$

For a mass spring system, the coupling coefficient is defined as [62]:

$$\kappa = \frac{k_m}{\sqrt{(k_1 + k_m)(k_2 + k_m)}} \tag{2.15}$$

We see this definition of the coupling coefficient maintains the scaling of the coefficient from 0 to 1. If we assume both resonators are identical ($q_1 = q_2 = q$ and $k_1 = k_2 = k$) then we can combine Eq. 2.14 and 2.15 to get an expression for κ. If we assume the weak coupling regime ($k_m \ll k$), then we can also approximate κ as a convenient ratio of electrical to mechanical properties.

$$\kappa = \frac{q^2}{q^2 + 2\pi\underline{\varepsilon}r^3 k} \approx \frac{q^2}{2\pi\underline{\varepsilon}r^3 k} \tag{2.16}$$

2.3.2 Analyzing the Coupling Coefficient

In order to get a first order estimate of what values of κ to expect, we analyze the well studied example of tubulin. Tubulin is a dimer protein made of α and β tubulin monomers, and is the constituent building block of microtubules. In physiological pH, each monomer carries

a free charge of five electrons and has a mass of 50 kDa [63]. Simulations of the stiffness of tubulin suggest a spring constant of approximately 3.5 N/m [64]. While any potential resonance of the tubulin protein is likely much more complex than a simple spring mass oscillator, this at least provides a first order estimate on realistic values of κ. We assume that the frequency is high enough to ignore the effects of conductivity in the medium, and assume a relatively close separation distance of 10 nm. Plugging in $k = 3.5$ N/m, $q = 8 \times 10^{-19}$ C, $\varepsilon = 80\varepsilon_0$, and $r = 10$ nm into Eq. 2.16, we find $\kappa = 4.12 \times 10^{-5}$. This small coupling would permit almost no energy transfer between resonators. Potential biological resonators therefore need a substantially greater charge density in order to permit stronger coupling.

2.3.3 Energy Transfer Between Coupled Resonators

Coupled mode theory provides an expression for the maximum possible power transfer efficiency between two coupled resonators, which can also be solved from circuit theory [65, 66].

$$\eta = \frac{\kappa^2 Q_1 Q_1}{(1 + \sqrt{1 + \kappa^2 Q_1 Q_2})^2} \tag{2.17}$$

For the rest of our analysis, we will assume the resonators are identical ($Q_1 = Q_2 = Q$). This means for a system transmitting power P_t, the power absorbed is given by $P_a = \eta P_t$. This expression assumes optimal impedance matching and represents the highest possible power transfer efficiency between the two resonators. From Eq. 2.5, we know the energy absorbed is given by $U_{max} = P_a Q / \omega$. By setting the maximum stored energy to thermal energy ($U_{max} = k_B T$) as done in Eq. 2.18, we can solve for Q to get an expression for the minimum necessary Q factor.

$$k_B T = \frac{\eta P_t Q}{\omega} \tag{2.18}$$
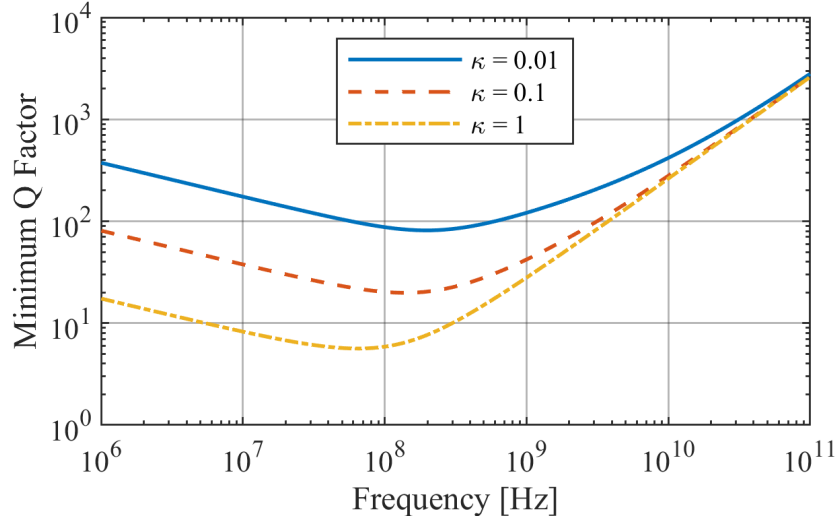
Figure 2.5: Minimum Q factor for two identical, coupled resonators as a function of frequency for different inter-resonator coupling strengths (κ). We assume $T = 300$ K and $P_t = 10^{-12}$ W. The value of κ in the legend is attenuated as a function of frequency by a factor of $|A(\omega)|$.

The explicit solution for Q in Eq. 2.18 is solvable, though complicated because η is also a function of Q. For sake of intuition, we can take a Taylor expansion of Eq. 2.17 about $\kappa = 0$ (for any significant interaction distance, $\kappa \ll 1$) and obtain an approximate solution.

$$Q_{min} \approx \sqrt[3]{\frac{4k_B T \omega}{P_t \kappa}} \tag{2.19}$$

Unlike the far field case, this expression for the minimum Q factor is frequency dependent.

The explicit (non approximate) form of Eq. 2.19 is plotted in Fig. 2.5 for varying values of coupling strength. The value of coupling coefficient in the legend is attenuated as a function of frequency by a factor of $|A(\omega)|$ where $A(\omega)$ is defined in Eq. 2.1. The medium is assumed to have a relative permittivity of 80 and a conductivity of 1.1 S/m. Using the same logic from the far field case, we limit the source power to the average power output of a cell, $P_t = 10^{-12}$ W [58]. We see the minimum Q factor is lowest near the plasma frequency, where the oscillation period is longer but the interacting fields are not yet screened.

2.4   Comparison with Simulated Resonances

We have established general criteria for a resonator to have the possibility of sustaining near or far field communication. Far field communication requires excessively high Q factors at non thermal power levels, and seems unlikely as a communication modality in general. Near field communication seems likely at frequencies near the plasma frequency, but coupling strengths would need to be particularly high to permit biologically realistic Q factors. To compare our criterion to more practical scenarios, we compare our near field limit to previously studied biological resonances.

2.4.1   Microtubule Vibrations

Microtubules have been extensively analyzed in terms of normal modes and vibrations. Microtubules are a ubiquitous component of the cytoskeleton and cilia of eukaryotic cells. They are tubular protein complexes constructed out of alpha and beta tubulin monomers. A considerable amount of research has been been spent studying the mechanical vibrations of microtubules [41, 67], and even the resulting electric fields that would be generated by the vibrating polar protein [40, 68, 42]. No experimental evidence to date has confirmed these high frequency vibrations. Various computational studies calculate vibrational frequencies on the order of 1 to 100 GHz, depending on length and material properties [41].

The Q factor of hypothetical microtubule resonances has unfortunately been overlooked by some computational studies. Some work suggests vibrations would be entirely overdamped by surrounding viscous media [69]. As a counter argument, Pokorný suggested that the ion layer around the charged surface of the microtubule would create a slip boundary condition, enhancing the Q factor [70]. Such slip boundaries have been considered analytically in nano-resonators [71]. Only recently has a computational study compared microtubule vibrations with multiple boundary conditions: no damping, no-slip layer, and slip layer [72]. Their results suggest that
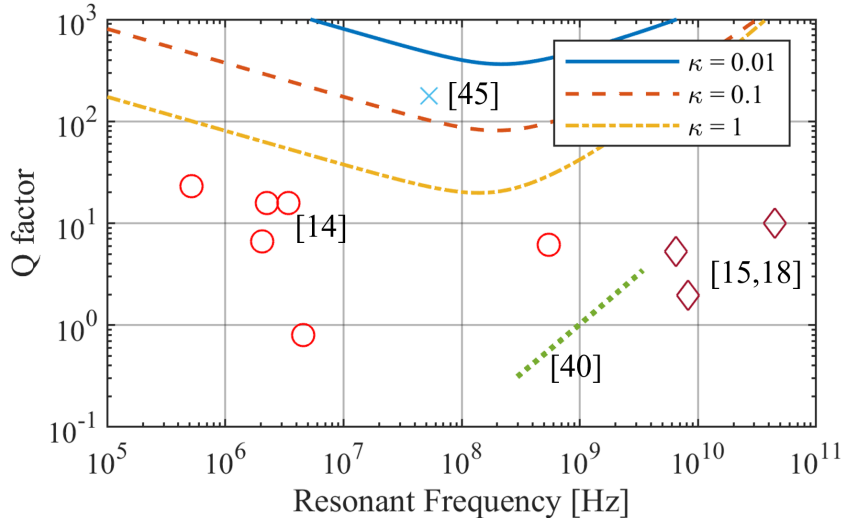
Figure 2.6: The minimum Q factor for near field communication (blue line) vs. frequency for varying values of κ. The red circles represent the Q factor of calculated bacteria cell membrane resonances for different bacterial species computed in [43]. The green dotted line represent the calculated Q factor of bending microtubule vibrations as a function of microtubule length computed in [67]. The cyan cross represents the Q factor of the slip layer radial mode calculated in [72]. Finally the magenta diamonds represent the Q factor of dipolar modes in viruses [44, 47].

with a no-slip boundary condition, all vibrational modes are overdamped. With the slip layer, only the flexing radial mode is underdamped because of its extremely low amplitude ($< 0.1\,\text{Å}$). The Q factor of this radial mode was calculated to be quite large: 177 at 53 MHz (S. Li, personal communication, October 11th, 2019). Because this is a radial mode, the resonant frequency is expected to be independent of length.

Another work computed the Q factor of the bending mode of microtubules with incident ultrasound waves using analytical beam equation methods [67]. They computed the resonant frequency and Q factor of the bending mode vibration of a $10\,\mu\text{m}$ microtubule as a function of mode number. It is expected that shorter microtubules should have higher resonant frequencies. Their data is reproduced and plotted alongside our minimum near field Q factor in Fig. 2.6.

2.4.2 Cell Membranes

Because of its negative charge, the cell membrane is also a candidate for electromechanical coupling. To explore ultrasound destruction of bacteria, Zinin investigated the Q factor of spherical bacterial cell membranes [43]. Using experimental data to inform cellular mechanical properties, they used an analytical model to estimate the resonant frequency and Q factor of several common bacteria. While some of these Q factors are quite large, most of these resonances are below the typical plasma frequency of cellular media. All of the reported Q factors are plotted alongside our minimum near field Q factor in Fig. 2.6. It should be noted that these modes were analyzed under the assumption of ultrasound excitation, and it is not guaranteed EM fields would couple into those modes.

2.4.3 Viruses

Many viruses are comprised of spherical or rod shaped capsid shells with negatively charged DNA or RNA inside. Recognizing the charge concentration in the center of viruses, work has been done investigating how microwaves could couple into the natural vibrational frequencies of the spherical or rod like "dipolar modes" in viruses [45]. These resonances have not only been modeled and simulated, but also measured experimentally and exploited to deactivate viruses at low power intensities [46, 47]. These measured Q factors are plotted in Fig. 2.6.

2.5 Conclusions

Starting with coupled mode theory relationships of energy transfer, we derived the minimum Q factors required for electromagnetic communication to occur between an incoming plane wave and resonator, as well as two resonators with coupled near fields. The key assumption is that the resonator must be able to store more energy from EM interactions than thermal energy. We identified a region where near field communication would be most efficient, might be sustained,
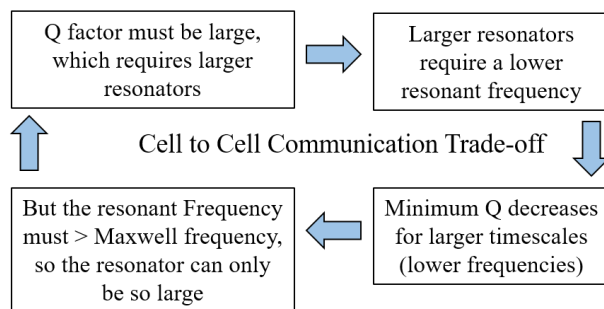
Figure 2.7: Diagram illustrating the fundamental trade-off of cell to cell communication using electrically coupled mechanical resonators. Essentially, the resonator must be large enough to maintain a large Q factor, but not so large as to resonate at a frequency below the plasma frequency.

occurring roughly around 100 MHz.

We compared our model with previous studies on the Q factor of microtubule, cell membrane, and virus vibrations. For microtubules, the Q factor of the bending modes is too low to meet our criteria for any coupling strength. The slip-layer radial mode is much more likely to sustain communication because of its large Q. The amplitude of the vibration simulated, however, was very small (< 0.1 Å), suggesting the mode might not be able to store much energy and that our transmit power might be an overestimate. Previous simulations on the flexing mode of microtubules have suggested it would be the most electrically active mode, but also that the mutual energy between vibrating microtubules would not exceed thermal energy [42].

Some cell membrane vibrations also have larger Q factors, but typically occur at too low of frequencies to meet our criterion for anything other that maximum coupling. The dipolar resonances of viruses on the other hand are at too high of frequencies to meet our criterion.

Our analysis suggests that high Q resonances centered around the plasma frequency have the greatest chance of sustaining cellular communication through electromechanical coupling. The simulated slip layer radial vibration in microtubules best meets our criterion. Our analysis also had an implicit power budget of $P_t = 10^{-12}$ W, which might be too large of an excitation to focus into a single microtubule and still vibrate within the slip layer. More research into the existence and properties of potential slip layers is required to explore its impacts on other

26

resonances.

This study reveals a fundamental trade-off for cell to cell communication via coupled resonators, which is illustrated in Fig. 2.7. Essentially, the resonator must be large enough to maintain a large Q factor, but so large as to resonate below the plasma frequency. This suggests the optimal frequency range for this modality of communication would be just above the plasma frequency for the media.

This chapter is based on "Limitations on electromagnetic communication by vibrational resonances in biological systems" KA Thackston, DD Deheyn, DF Sievenpiper. Physical Review E 101 (6), 062401. The dissertation author was the primary author of this material.

Chapter 3

Simulation of Electric Fields Generated from Microtubule Vibrations

Microtubules are ubiquitous organelles, appearing in the cytoskeleton of eukaryotic cells. They are tubular protein complexes constructed out of alpha and beta tubulin monomers. Microtubules are highly conserved across different species, and important for functions such as maintaining cell structure, intracellular transport, and cell division [26]. Researchers have spent considerable effort investigating and simulating the high frequency (>kHz) mechanical vibrations naturally exerted by microtubules [41]. One motivation behind this research is the theory that vibrating microtubules are the source of endogenous electric fields, which may serve some biological function [1, 73, 74, 75]. The constituent protein tubulin has a net dipole moment, and the arrangement of tubulin in the microtubule is such that the microtubule strand actually has a net dipole moment along its axis. Therefore, the motion of these tubulin proteins would generate alternating electric fields inside the cell.

To date, no experimental evidence has confirmed these high frequency vibrations. Simulation results are mixed in their findings. Many of these computational studies calculate vibrational frequencies on the order of 1 to 100 GHz. These resonant frequencies are dependent on the

microtubule length, as are the material properties of the microtubules themselves [41]. One work that used molecular dynamics to identify the normal modes of the microtubule noted that all modes other than flexing (the resonant frequency of which was not dependent on microtubule length) seemed to have lower resonant frequencies for longer microtubules [64]. They also noted that mode number was not length dependent for bending and twisting modes, while axial mode number decreased with increasing length, and flexing mode number increased with increasing length. An approximate model describing microtubule resonant frequency as a function of length is found in [68].

Even if microtubules were able to sustain high frequency mechanical vibrations, however, their ability to generate significant electric fields is not clear. Previous work has modeled electric fields from microtubules undergoing optical branch axial vibrations based on the vibrational analysis of Pokorný [76, 77]. These studies have modeled different arrangements of microtubules using what they have named the Microtubule Resonance Dipole Network Approximation method [40, 60, 78, 68].

These previous electric field simulations have only modeled one of the hypothesized vibrational modes from microtubules, namely the optical branch axial vibration. Additionally, it has not been thoroughly investigated whether such theoretical fields could have any biological significance. In this chapter, we use a transient method to simulate the electric fields from multiple vibrations (optical branch axial, acoustic branch axial, bending, twisting, and flexing). As in other biophysics work, we determine the field strength to be significant when it can interact with a potential energy greater than the background thermal energy [59]. We also evaluate the ability of microtubules to induce vibrations on one another based on their interaction energy.

3.1 Simulation Methods

In this chapter, we will use a numerical transient method to determine the fields generated by microtubule vibrations. Our model is transient in contrast to previous, frequency domain models. We simulate the trajectory of each tubulin monomer over the course of two vibrational periods in discrete time steps. Our model treats each tubulin monomer as a point dipole and sums the field contributions from each one as they move according to a given equation of motion.

3.1.1 Seeding the Microtubule System

The electromagnetic properties of tubulin and the geometric arrangement of tubulin in the microtubule are fortunately well studied. Although microtubules can be up to 50 µm long, most microtubules are 0.5 µm to 2 µm [26]. The hollow tube of a microtubule has an inner diameter of approximately 15 nm and an outer diameter of approximately 23 nm. In vivo, they consist of 13 protofilaments which wrap around the microtubule with an 8 nm pitch, as depicted in Fig. 3.1. Typically microtubules form a lattice of tubulin dimers in either the "13A" or "13B" configuration [79]. For the purposes of electric field generation, we have no reason to suspect one lattice type should be more electrically active than the other. In this chapter, we will consider the "13B" lattice type.

The electrical properties of the alpha and beta tubulin monomers are taken from molecular dynamics simulations and listed in Table **??** [63]. The dipole moment directions are defined in cylindrical coordinates, as labeled in Fig. 3.1. The z direction is along the axis of the microtubule, the r direction is directed radially away from the microtubule center, and the θ direction is tangential to the microtubule surface. Note that while the microtubule does have a net dipole moment along its axis, the radial component of tubulin's dipole moment is the greatest.

Table 3.1: Dipole moments of tubulin. Note the direction of the dipole moments is presented in cylindrical coordinates. Direction of dipole moments defined in Fig. 3.1.

Tubulin Dipole Moment (Debye)	α monomer	β Monomer
P_z	115	222
P_r	554	1115
P_θ	-6	-192
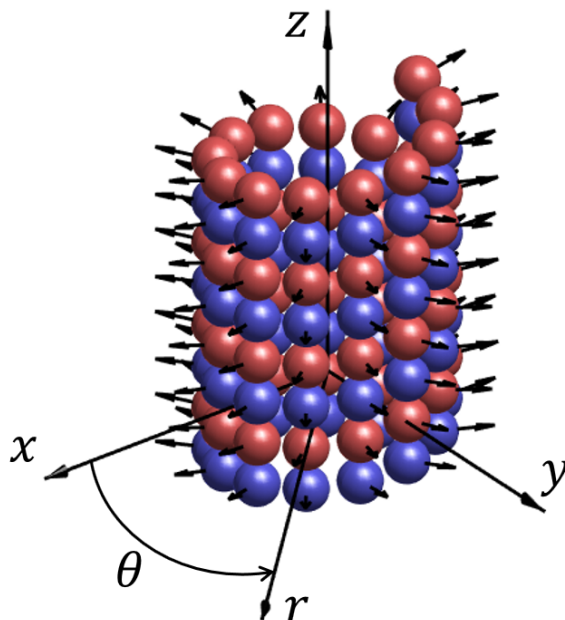
Figure 3.1: Three dimensional structure of a microtubule. Red spheres indicate alpha tubulin and blue spheres indicate beta tubulin. The black arrows show the dipole moment of each tubulin monomer.

3.1.2   Motion of the Microtubule

We simulate five modes of vibrations that have been hypothesized or simulated in previous works. The first four are acoustic branch vibrations: axial, bending, flexing, and twisting [80]. The fifth mode is an axial vibration on the optical branch [76]. The two constituent particles in the microtubule lattice are the alpha and beta tubulin monomers. In acoustic branch vibrations, these monomers move coherently, whereas in optical branch vibrations they move out of phase [81].

For this reason we simulate alpha and beta monomers independently, instead of looking at just the tubulin dimer. Traditionally, optical branch vibrations are considered more electromagnetically active than acoustic branch vibrations, hence the focus on optical branch vibrations in past works.

The equations of motion for each mode follow the form of:

$$\xi_i(t) = A \sin(\omega t) \sin\left(\frac{n\pi z_{i0}}{L}\right) + \xi_0 \tag{3.1}$$

Where A is the amplitude of the vibration, ω is the angular frequency of the vibration, n is the order of the mode, L is the length of the microtubule, $\xi_i(t)$ is the coordinate dependent on the mode of vibration of node i as a function of time, ξ_0 is that same coordinate at $t = 0$, and z_{i0} is the z coordinate at $t = 0$. Every alpha and beta monomer constitutes its own node. The axial, bending, flexing, and twisting modes represent vibrations along the z, x, r, and θ coordinates respectively (assuming the microtubule is aligned on the z axis, with the base at $z = 0$ and the top at $z = L$, as shown in Fig. 3.1). In twisting vibrations, the amplitude is scaled to the microtubule radius such that the amplitude of θ corresponds to the arc length swept. For the optical branch vibration, the beta tubulin monomers are vibrating out of phase with the alpha monomers along the z axis. The motion of Eq. 3.1 fixes the end points of the microtubule, which would be expected in many biological settings.

Additionally, our simulation applies rotation matrices to the dipole moment of each node at every time step to simulate the deformation of the microtubule. Node i remains in the same orientation to the node directly above it (node $i + 13$). These rotation matrices are given by Eq. 3.2 and Eq. 3.3, and the angles of rotation are given by Eq. 3.4.

$$[R_x] = \begin{bmatrix} 1 & 0 & 0 \\ 0 & \cos\theta_x & -\sin\theta_x \\ 0 & \sin\theta_x & \cos\theta_x \end{bmatrix} \tag{3.2}$$
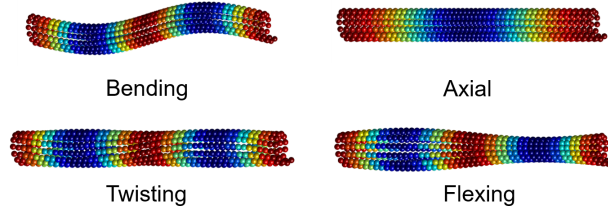
Figure 3.2: Bending, axial, twisting, and flexing microtubule vibrations (left to right, top to bottom). Amplitudes are exaggerated for the purposes of illustration. All vibrations are second order ($n = 2$ in Eq. 3.1.

$$[R_y] = \begin{bmatrix} \cos\theta_y & 0 & \sin\theta_y \\ 0 & 1 & 0 \\ -\sin\theta_y & 0 & \cos\theta_y \end{bmatrix} \tag{3.3}$$

$$\theta_x = -\tan^{-1}\left(\frac{\Delta y}{\Delta z}\right), \theta_y = \tan^{-1}\left(\frac{\Delta x}{\Delta z}\right) \tag{3.4}$$

The lengths of Δx, Δy, and Δz are defined as the differences in the x, y, and z coordinate respectively between node i and node $i + 13$. Thus the dipole moment of any node as a function of time is given by Eq. 3.5.

$$\vec{p}_i(t) = [R_y][R_x]\vec{p}_{i0} \tag{3.5}$$

Illustrations of the four acoustic modes, with exaggerated amplitudes, are shown in Fig. 3.2.

3.1.3 Fields from Microtubule

Because we only consider distances much less than the expected wavelength ($\ll 1$ mm), we calculate the total fields using a quasi-static approximation. The electrostatic field from each dipole is summed at every discrete time point in a particular point in space, with the field expression given by Eq. 3.6 [82].
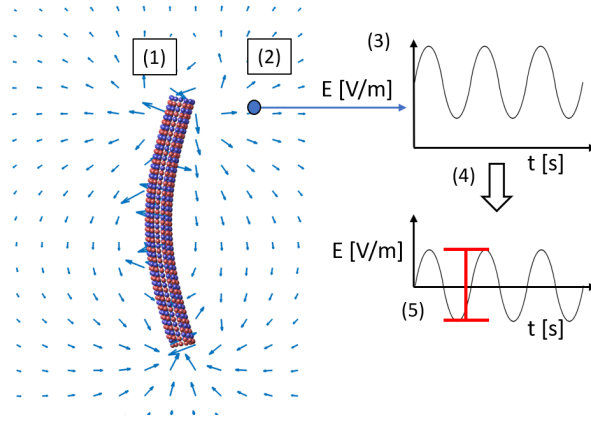
Figure 3.3: Procedure for numerically calculating the E field strength in conductive media for arbitrary vibrations: (1) Move dipole moments along predetermined motion. (2) Sum fields from all nodes at particular point in space. (3) Get E field vs. time for one point in space. (4) Remove DC component. (5) Extract peak to peak E field.

$$\vec{E} = \frac{3\hat{r}(\hat{r} \cdot \vec{p}) - \vec{p}}{4\pi\varepsilon r^3} \tag{3.6}$$

Where $\vec{E}$ is the electric field strength in V/m, $\vec{p}$ is the vector dipole moment in C m, ε is the permittivity of the medium, and $\vec{r}$ is the distance vector pointing from the center of the dipole to the observation point. In order to enforce the screening effect of the media, which is discussed in greater detail in Section 2.1, we simulate the total transient fields at some point in space for a few periods. We remove the DC offset of the field to account for screening and calculate the peak-to-peak electric field strength. This peak-to-peak value is taken as the strength of the E field in the medium. A flowchart depicting how we calculate the electric field in space from the moving microtubules is shown in Fig. 3.3.

When we calculate the potential energy in an electric field, we use Eq. 3.7.

$$U = -\vec{p} \cdot \vec{E} \tag{3.7}$$

Where U is the potential energy. When we calculate the potential energy between microtubules, we sum the absolute value of the potential energy of every tubulin dimer in

the receiving microtubule system in the presence of the fields generated by the transmitting microtubule.

3.1.4 Comparison with Microtubule Resonance Dipole Network Approximation

Our results are slightly different from previous simulations using the Microtubule Resonance Dipole Network Approximation [40, 60, 78, 68], which models the the oscillating tubulin as a Hertzian dipole. Here we argue this is not an accurate approximation at larger distances. Just as the time varying fields from an oscillating charge look like a Hertzian dipole, the time varying fields from an oscillating dipole should look like a Hertzian quadrapole. To demonstrate this, let us examine the electric field along the z axis given by a dipole oriented and moving up and down along that same axis.

$$E = \frac{2p}{4\pi\varepsilon\left(r + A\sin(\omega t)\right)^3} \tag{3.8}$$

Where p is the magnitude of the dipole moment, r is the distance between the observation point and the dipole, A is the amplitude of the oscillation, ω is the angular frequency of vibration, and t is time. If we assume $r \gg A$, we can take the first two terms of the Taylor series expansion of Eq. 3.8. This isolates the principle component of the time varying fields.

$$E \approx \frac{2p}{4\pi\varepsilon r^3} - A\sin(\omega t)\frac{6p}{4\pi\varepsilon r^4} \tag{3.9}$$

The first term in Eq. 3.9 represents the DC component of the fields, while the second term is time dependent. The time varying fields decay as a power of r^{-4}, similar to a Hertzian quadrapole. In conductive media, the DC and low frequency components are screened, as described in Sec. 2.1. Modeling each oscillating tubulin as a Hertzian dipole is therefore overestimating the distance of interaction. We believe our quasi-static transient simulation, which

35

removes the DC fields numerically, is a more accurate simulation.

3.2 Results

The key parameters we can sweep in our simulation are the vibration type, mode number, vibration amplitude, the length of the vibrating microtubule, and of course where in space we are measuring field strength. As discussed in Sec. 2.1, we will not consider the impact of vibration frequency as we are only studying near fields from vibrations occurring beyond the Maxwell frequency.

In past works considering the biological effects of electromagnetic fields, significant interaction was deemed to occur at interaction energies greater than thermal energy (k_BT), or with forces on the order of $1\,\text{pN}$ [59]. The largest dipole moment for a single protein cataloged by [83] is 34,460 Debye (or $1.232 \times 10^{-25}\,\text{Cm}$). From Eq. 3.7, we can determine the E field necessary to have a potential energy equal to thermal energy (k_BT). Assuming a temperature of $300\,\text{K}$, the E field would need a magnitude of $3.36\,\text{kV/m}$. The same database catalogs the largest free charge of any single protein at 446 e. To exert a force of $1\,\text{pN}$ would require $1.4\,\text{kV/m}$. This suggests that biologically significant fields must be on the order of $1\,\text{kV/m}$. Here we only consider traditional electromagnetic interaction, ignoring more exotic effects such as stochastic resonance at the receiver which could allow for the reception of weaker signals.

3.2.1 Electric Field from Different Vibration Types

The vibration types studied here are axial, bending, flexing, and twisting modes, as well as optical branch axial vibrations. These are typical normal modes for hollow cylinders and the modes identified in previous computational studies [80]. Any microtubule vibration would consist of some superposition of these modes. Numerical studies suggest all modes have lower resonant frequencies for longer microtubules, except for the flexing mode which has been identified to
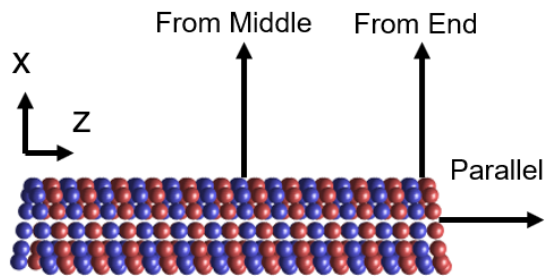
Figure 3.4: The three different lines along which we plot the E field.

have a resonant frequency independent of length at about $100\,\text{GHz}$, presumably because the relevant length scale is the microtubule diameter [64]. At these frequencies our model may slightly underestimate the electric fields because the dielectric of cytosol will become frequency dependent.

For comparison of vibration type, we simulate the electric field strength as a function of distance perpendicular to the microtubule axis from its middle and end, and distance parallel to the end of the microtubule (illustrated in Fig. 3.4). All simulations are performed for $1\,\mu\text{m}$ long microtubules with $0.1\,\text{nm}$ amplitude vibrations (a typical vibration amplitude according to molecular dynamics works [64]). All vibrations are of the first order ($n = 1$). The dielectric of the media is 80. These results are plotted in Fig. 3.5. Interestingly, the flexing vibration, which has not been electrically modeled in past works, produces the strongest fields.

3.2.2 Electric Field from varying Mode Order

As the flexing mode produces the strongest fields, we also examine the strength of the E fields for varying mode order in Fig. 3.6. It has been observed in simulation that mode number was not length dependent for bending and twisting modes, while axial mode number decreased with increasing length, and flexing mode number increased with increasing length [64]. It can be seen that increasing the mode order increases the field strength at close distances, but tends to decrease the field strength at distances that are larger than the scale of the microtubule ($1\,\mu\text{m}$). This trend holds for most other vibrational modes.
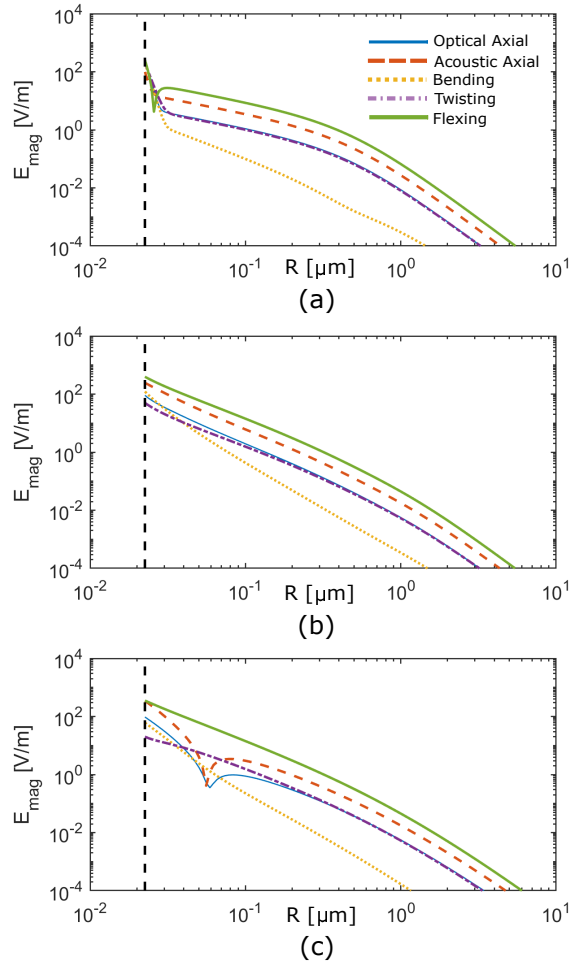
Figure 3.5: The magnitude of the time varying E fields coming from different vibration types. Plot (a) shows distance normal to the microtubule from the middle, (b) shows distance normal to the microtubule from the end, and (c) shows distance parallel to the microtubule from the end. The black dotted line shows the surface of the microtubule. For all plots, $L = 1\,\mu m$, $n = 1$, and $A = 0.1\,nm$.

3.2.3 Electric Field as a function of Amplitude

The previous results were simulated with a vibration amplitude of 0.1 nm, on the order predicted by molecular simulation [64]. The same molecular simulations make the intuitive conclusion that amplitude would decrease as vibrational frequency increases, and increase as microtubule length increases. An extrapolated model relating microtubule resonant frequency to
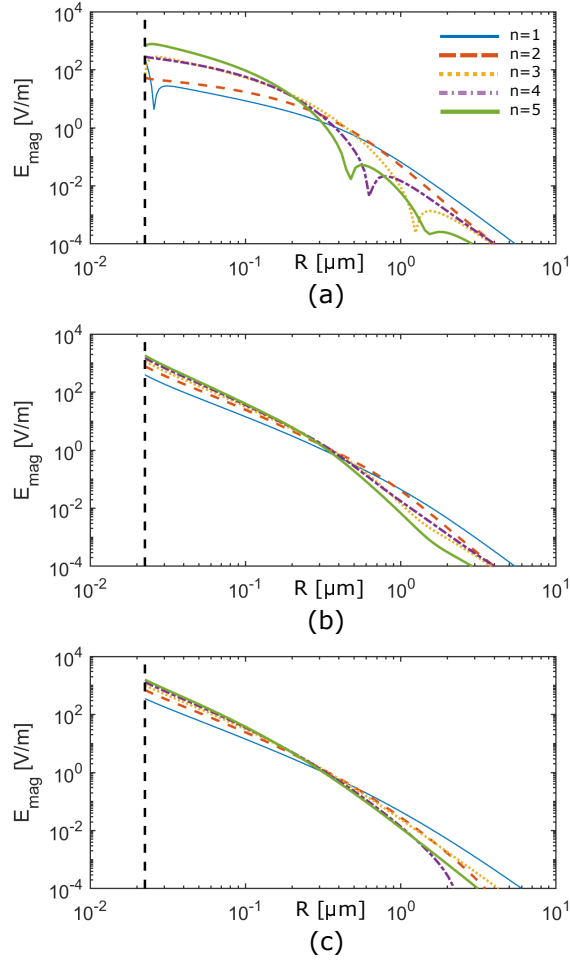
Figure 3.6: The magnitude of the time varying E fields from a flexing microtubule for different orders of vibration ($n = 1, 2, ...5$). Plot (a) shows distance normal to the microtubule from the middle, (b) shows distance normal to the microtubule from the end, and (c) shows distance parallel to the microtubule from the end. The black dotted line shows the surface of the microtubule. For all plots, $L = 1\,\mu m$ and $A = 0.1\,nm$. We see there are some dips for higher order modes in (a). This is likely from higher order modes resulting in fields that cancel out at certain distances due to complex multipoles.

length suggests that at lengths larger than $20\,\mu m$, the resonant frequency begins to dip below the Maxwell frequency of $250\,MHz$ [80].

To investigate the effects of the amplitude, we plot the electric fields for different amplitudes of the flexing mode from $0.1\,nm$ - $1\,nm$ in Fig. 3.7. While longer microtubules should be
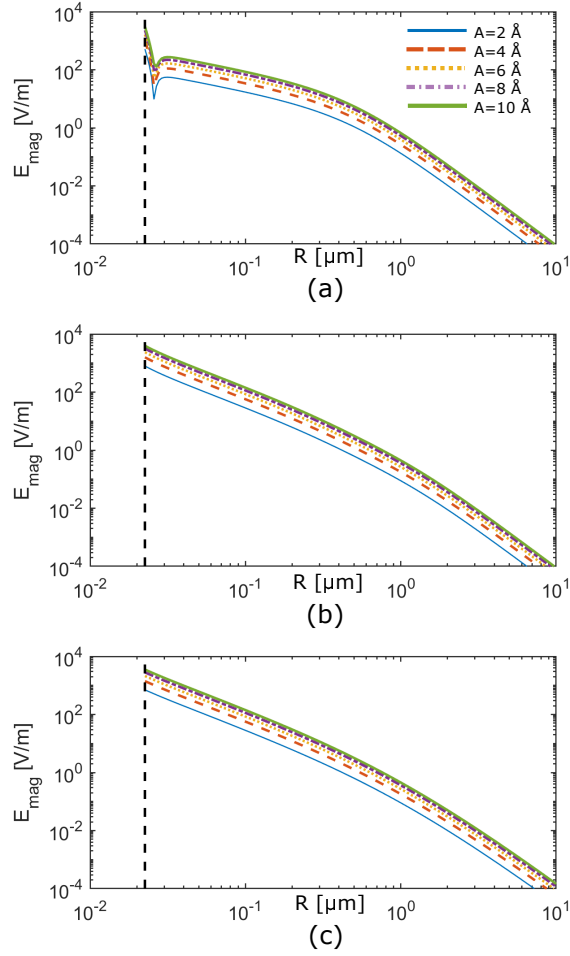
Figure 3.7: The magnitude of the time varying E fields from a flexing microtubule for varying vibration amplitudes ($A = 200\,\text{fm}, 400\,\text{fm}, 600\,\text{fm}, 800\,\text{fm}, 1000\,\text{fm},$). The black dotted line shows the surface of the microtubule. For all plots, $L = 1\,\mu\text{m}$ and $n = 1$.

able to sustain larger amplitudes, vibrations larger than 1 nm seem unlikely without damaging the microtubule. Additionally, we plot the E field at a single point 1 μm from the middle of flexing microtubule as a function of vibrational amplitude Fig. 3.8. As expected from Eq. 3.9, the magnitude of the E field increases linearly with amplitude.
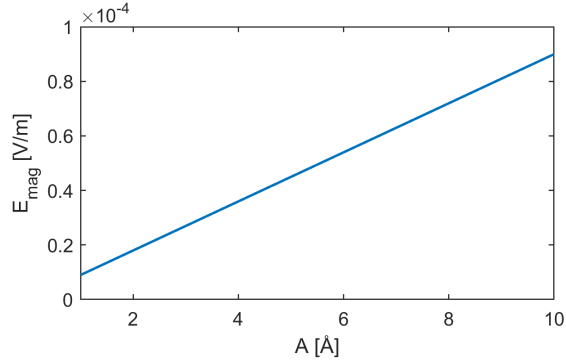
Figure 3.8: The magnitude of the time varying E fields a flexing microtubule as a function of vibration amplitude. $L = 1\,\mu m$ and $n = 1$.

3.2.4 Potential Energy between Two Microtubules

The previous results suggest it would be difficult for the electric fields from a single vibrating microtubule to have significant long range interactions on other biomolecules. To address the question of whether mechanical vibrations in one microtubule could induce vibrations in a neighboring microtubule, we evaluate the potential energy between two microtubules using the process described in section 3.1.3. We simulate the potential energy between two shorter microtubules (100 nm long) because the simulation time of our potential energy simulation increases as a function of L^2.

We consider two different orientations: two microtubules side by side, and two micro-tubules along the same axis, as illustrated in Fig. 3.9. Results are shown for the case of a first order flexing mode with 0.1 nm amplitude vibrations in Fig. 3.10.

3.3 Analytical Model of Potential Energy Between 2D Micro-tubules

To give some understanding on the relationship between microtubule length and mutual energy, we derive an analytical model of the mutual energy per unit length between two infinite,
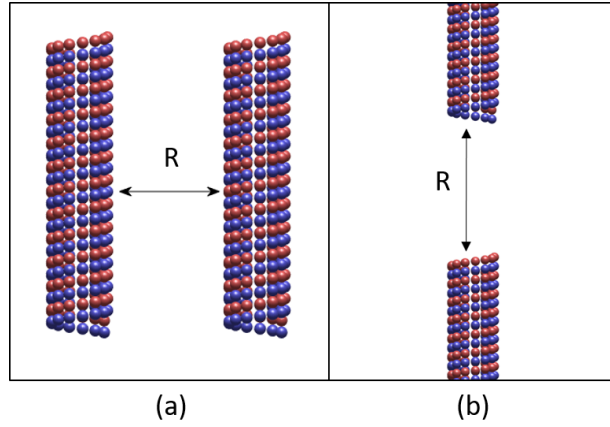
Figure 3.9: Illustration showing two 100 nm microtubules in parallel (a) and in series (b).
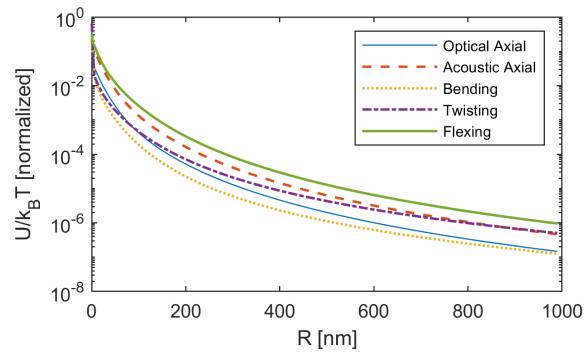
Figure 3.10: The interaction energy between two microtubules in parallel as a function of distance. $L = 100\,\text{nm}$, $n = 1$, and $A = 0.1\,\text{nm}$.
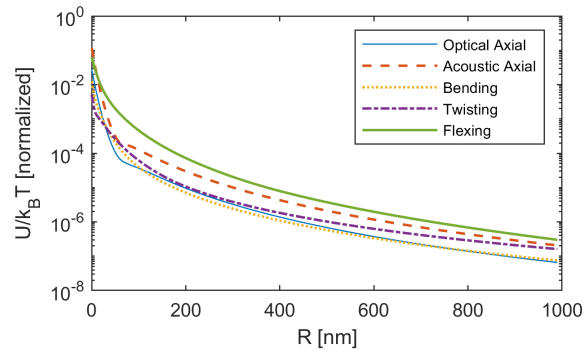
Figure 3.11: The interaction energy between two microtubules in series as a function of distance. $L = 100\,\text{nm}$, $n = 1$, and $A = 0.1\,\text{nm}$.

2D microtubules. A sketch of the problem is shown in Fig. 3.12.

As discussed in section 3.1.4, a dipole moving up and down along its axis creates time
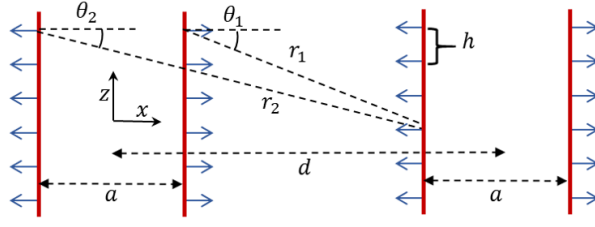
Figure 3.12: Diagram of the 2D microtubule. Blue arrows represent the radial component of the tubulin dipole. Microtubules have a diameter of a and a separation distance of d.

varying fields that look like a linear Hertzian quadrapole with a quadrapolar moment given by $Q = Ap$ where A is the amplitude of oscillation and p is the dipole moment. We will model the source as two infinite linearly distributed quadrapoles, where the periodic time dependence is considered implicit. The electric potential from a quadrapole aligned is given by 3.10.

$$V = \frac{Q}{4\pi\varepsilon r^3}(3\cos^2\theta - 1) \tag{3.10}$$

Assuming that the microtubule on the left of Fig. 3.12 is vibrating in the flexing mode (i.e. the dipoles are oscillating along the x axis), we can integrate along the length of microtubule to find the field contribution. Unlike in our numerical simulation, the ends of these microtubules are not fixed, since that would not be meaningful for the infinite case. We can replace Q in 3.10 with a differential quadrapole moment per unit length given by $\lambda = Ap/h$. Here h is the height of the dipole, in this case 8 nm. The total potential from one side is therefore given by the integral shown in 3.11.

$$V_i = \int_{-\infty}^{\infty} \frac{\lambda}{4\pi\varepsilon r_i^3}(3\cos^2\theta_i - 1)\mathrm{d}z, \, i = 1,2 \tag{3.11}$$

$$\cos\theta_1 = \frac{x-a}{r_1}, \, \cos\theta_2 = \frac{x+a}{r_2} \tag{3.12}$$

$$r_1^2 = (x-a)^2 + z^2, \, r_2^2 = (x+a)^2 + z^2 \tag{3.13}$$

43

The total potential is simply the sum of the two sides, $V_{MT} = V_1 + V_2$. The electric field is given by $\vec{E} = -\nabla V_{MT}$ and has only an x component.

$$E_x(x) = \frac{\lambda}{4\pi\varepsilon} \frac{8x(x^2 + a^2)}{(x^2 - a^2)^3} \tag{3.14}$$

Using 3.7 as an expression for the potential energy, we can determine the potential energy per unit length for two neighboring microtubules by summing the potential experienced by the left and right side of the microtubule.

$$\bar{U} = \left[E_x(d - a) - E_x(d + a) \right] p/h \tag{3.15}$$

After using 3.14 to solve 3.15 and recalling our earlier definition of λ, we can solve for the potential energy per unit length from an infinite vibrating microtubule as a function of separation distance.

$$\bar{U} = \frac{1}{4\pi\varepsilon} \frac{Ap}{h} \frac{16p(3ad^2 + 4a^3)}{h(d^2 - 4a^2)^3} \tag{3.16}$$

We observe that for cases where $d \gg a$, the potential energy is decaying to the power of d^{-4}, similar to what was predicted by our numerical case. We expect interaction energy to increase approximately linearly with microtubule length. When plotting 3.16, we use the numerical values of $p = 1669$ Debye, $h = 8$ nm, $A = 0.1$ nm, $\varepsilon = 80\varepsilon_0$, and $a = 23$ nm.

3.4 Discussion and Conclusions

3.4.1 Different Vibration Types

Earlier we discussed that if an electric field was to interact with biomolecules in any conventional fashion, it would need to be on the order of $1\,\text{kV/m}$ to overcome thermal energy.

In Fig. 3.5 we see that none of the different vibration types achieve fields of that strength for any distance from the microtubule surface. Interestingly, we see the flexing mode is the most electromagnetically active, which has not previously been simulated. This makes sense when noting in table **??** that the radial component of tubulin's dipole moment is strongest.

Previous works have noted that the axial vibration types are considered the most mechanically likely because they would displace the least fluid and are less likely to be damped [41]. It is also interesting to note that the acoustic axial vibration produces fields stronger than the optical branch axial vibration. Conventional wisdom holds that optical branch vibrations should be more electrically active, and this is true when the constituent particles in the lattice are positive and negative charges. The α and β tubulin monomers, however, are dipole moments both with positive z components, instead of opposing charges.

3.4.2   Varying Mode Order and Vibrational Amplitude

Because the flexing mode produced the strongest fields, we evaluated it for different mode orders in Fig. 3.6. In general we see increasing the mode order results in stronger fields close to the surface of the microtubule, but weaker fields at distances larger than the length of the microtubule. This suggests that the higher order modes would not be useful for long distance interactions.

A physical interpretation of these results is that as the mode order increases, the moment of the effective multipole increases. At distances larger than the length of the microtubule, the vibration should look like a point multipole with some moment proportional to the order of the vibration. As this moment increases, so too will the power at which the fields decay over distance, resulting in weaker fields at distances larger than the length of the microtubule. We also see some dips in the E field around the 1 μm distance only for higher mode orders in the top plot of Fig. 3.6. We infer this is a location where the field contributions from out of phase oscillations becomes destructive and results in a weaker field.

In Fig. 3.7 and 3.8, we swept the vibrational amplitude of the flexing microtubule. As predicted by Eq. 3.9, the field strength increased linearly with the amplitude. For both the mode order and amplitude sweep, we start to see fields approaching $1\,\mathrm{kV/m}$ at distances on the order of 10-100 nm, significantly longer than the Debye length.

3.4.3   Potential Energy Between Two Microtubules

In Fig. 3.10 and 3.11, we simulated the potential energy between two small microtubules for separation distances up to $1\,\mu\mathrm{m}$. As expected, interactions are strongest for the flexing mode. Even when the microtubules are in contact, however, the electric potential energy still cannot surpass the background thermal energy. This suggests it is unlikely that mechanical vibrations in one microtubule could induce vibrations in a neighboring microtubule through electric field interaction.

One issue with this method of simulation is that the mutual energy between two microtubules is dependent on the length of the microtubule. Our simulation method, however, scales in computation with the square of the microtubule length, making simulations of larger microtubules time consuming. Instead of simulating longer microtubules, we derive an analytical model of the potential energy per unit length between two infinite microtubules. The details of the derivation are found in Appendix 3.3. In Fig. 3.13 we see the models show strong agreement. Two important trends to note from this are that the potential energy decays as a function of r^{-4}, and that potential energy between two microtubules scales linearly with length. We see that in order for two microtubules about 50 nm apart to interact above thermal energy in these conditions, the microtubules would have to be approximately $10\,\mu\mathrm{m}$ long.
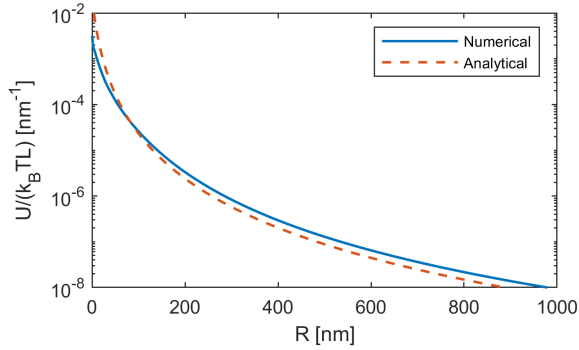
Figure 3.13: The interaction energy (normalized to thermal energy) per unit length (nm) between two microtubules in parallel as a function of separation distance. The transmitting microtubule is vibrating in the flexing mode. The numerical simulation is from simulating 100 nm long microtubules, while the analytical model assumes the infinite case (see Appendix 3.3 for more information on the analytical model).

3.4.4 Summary

We have presented a new method for simulating the electric fields from vibrating microtubules. Our method is capable of simulating any vibrational mode and sweeping a variety of parameters. Based on conventional definitions of interaction, we did not identify any cases where the fields produced by the microtubule could interact with biomolecules at large distances ($>$ 100 nm), though there are cases with high vibrational order and amplitude that could achieve fields exceeding 1 kV/m on distances that are at least larger than the Debye length. If these fields were to have any biological significance, they would more likely be for short distance, intracellular regulation, instead of inter-organism communication. Other factors such as multiple coherent microtubules, stochastic resonance at the receiver, or atypical interactions with the media are left outside the scope of this chapter.

This chapter is based on "Simulation of electric fields generated from microtubule vibrations" KA Thackston, DD Deheyn, DF Sievenpiper. Physical Review E 100 (2), 022410. 2019. The dissertation author was the primary author of this material.

Chapter 4

Modeling Electrodynamic Interactions in Brownian Dynamics Simulations

Molecular simulation is a powerful tool for the study of biomolecules, allowing researchers to learn about the structure of proteins, discover new drugs, and predict the impact of environmental factors on biological function. Because of the ubiquity of electromagnetic (EM) fields in our daily life, there has long been research in EM interactions with biomolecules. The modern consensus is that any significant interaction would be thermally driven, but there is significant interest in potential non-thermal EM interactions with biomolecules [59, 84].

All-atom molecular dynamics (AA-MD) is a simulation technique in which every atom in the system is explicitly simulated, including the solvent. This method can be very effective for simulations for time scales less than $1\,\mu s$ and for length scales less than $100\,nm$ [85]. For larger structures, such as chromatin or microtubule bundles, this method is not always feasible. Brownian Dynamics (BD) is a computational method that reduces complexity by modeling the solvent as a continuum [86]. By only taking into account large or coarse grained bodies, this method can access much greater time and length scales than AA-MD at the expense of accuracy.

When accounting for electric field interactions between charges, however, BD simulations

make an electrostatic assumption. An ionic medium is characterized by a Debye length, which characterizes the thickness of the counter-ion cloud around a charged body [51]. Macroscopically, the Debye length is related to the conductivity of the medium. Within the medium, electrostatic fields decay exponentially as a function of the Debye length. At sufficiently high frequencies, however, endogenous fields can become long range and overcome the attenuation by the ionic medium [53]. This is because beyond the Maxwell frequency (or plasma frequency) of the medium, the ions no longer have the mobility to keep up with the alternating fields and the medium appears non-conductive. For cellular media, the Debye length is often on the order of 1 nm and the Maxwell frequency is approximately 250 MHz [52].

The electrostatic assumption in BD, therefore, assumes that electric field interactions are occurring on time scales much longer than the relaxation time of the medium. For high frequency or high power pulse applications, this is not always the case. All atom MD would be able to account for this physics because medium properties such as Debye lengths, conductivity, and permittivity are all emergent properties of atomic interactions. To our knowledge, however, there is no method to take into account electrodynamic interactions in BD simulations.

In this chapter, present a method to explicitly account for electrodynamic interactions in a BD simulation. This method does not require explicit simulation of the background solvent nor a lattice to compute local ionic concentrations. Analyzing the continuum system, we derive an expression for the charge density of the ionic wake of a moving charge. Using this method, we propose a method where the ionic wake is represented with a finite exponentially decaying series of point charges. We compare this method to the known solution for an oscillating dipole embedded in a conductive medium to demonstrate its accuracy. We believe this simulation technique could be useful for those studying high frequency or high power electric field interactions with biological systems, such as electroporation or tumor treating fields [87, 84, 88].

4.1 Representation of a Moving Charge in Conductive Media

To derive an expression for the charge density representing a moving charge in conductive media, we revisit Tai's treatment of the electrodynamics of sources with moving media, which is of course a coordinate transformation of a moving source [89, 90]. In particular, Kalafus performed a study on the Cerenkov radiation from charges moving through conductive media, a treatment which is useful for us even at non-relativistic speeds [91]. Our goal will be to define the charge density of a moving charge in conductive media. The charge is assumed to be insulated so that the source charge is non-dissipating.

4.1.1 Source and Response Charge Charge Densities

When analyzing electrodynamics in conductive media, special attention must be paid to the accounting of charge density. In particular, we find the need to define separate source and response charge density terms. To demonstrate this we start with a formulation of Ohm's Law.

$$\vec{J} = \vec{J}_v + \sigma \vec{E} \tag{4.1}$$

Where $\vec{J}$ is the total current density, $\vec{J}_v$ is the convection current density, σ is the conductivity of the medium, and $\vec{E}$ is the electric field. If we take the divergence of Eq. 4.1, we can use the constitutive relationships $\nabla \cdot \vec{D} = \rho$, $\vec{D} = \varepsilon \vec{E}$, and the continuity relationship $\nabla \cdot \vec{J} = -\frac{\partial \rho}{\partial t}$ to obtain Eq. 4.2.

$$-\frac{\partial \rho}{\partial t} = \nabla \cdot \vec{J}_v + \frac{\sigma}{\varepsilon} \rho \tag{4.2}$$

Now let us analyze the case of some constant charge density moving at some constant velocity v along the z axis. One is tempted to define the convection current as $\vec{J}_v = \rho \vec{v}$. Such a definition, however, results in Eq. 4.2 being valid only for the trivial case of $\rho = 0$. Thus we must actually decompose the total charge density into the source (ρ_s) and response (ρ_r) terms and

define the convection current in terms of the source charge density.

$$\rho = \rho_s + \rho_r \tag{4.3}$$

$$\vec{J}_v = \rho_s \vec{v} \tag{4.4}$$

Physically we can interpret the source term as the moving charge density, and the response term as a counter-ion wake left behind by the moving source charge density. Next we must define this new response term ρ_r. Substituting Eq. 4.3 and 4.4 into Eq. 4.2, we obtain:

$$\frac{\partial \rho_r}{\partial t} + \frac{\sigma}{\varepsilon}\rho_r = -\nabla \cdot (\rho_s \vec{v}) - \frac{\partial \rho_s}{\partial t} - \frac{\sigma}{\varepsilon}\rho_s \tag{4.5}$$

The divergence term in Eq 4.5 can be simplified by using a vector calculus identity:

$$\nabla \cdot (\rho_s \vec{v}) = \vec{v} \cdot \nabla \rho_s + \rho_s (\nabla \cdot \vec{v}) \tag{4.6}$$

If we assume the source charge is moving at a constant velocity, the second term on the right goes to zero and the first term becomes $\vec{v} \cdot \nabla \rho_s = -\frac{\partial \rho_s}{\partial t}$.

Equation 4.5 then simplifies to Eq. 4.7, which is the general differential equation relating the source and response charge density terms.

$$\frac{\partial \rho_r}{\partial t} + \frac{\sigma}{\varepsilon}\rho_r = -\frac{\sigma}{\varepsilon}\rho_s \tag{4.7}$$

4.1.2   Time Independent Solution for Moving Point Charge

Equation 4.7 can be solved explicitly for ρ_r by applying a Lorenzt transformation and moving to a measurement frame where the charge density is stationary and the media is moving at a constant velocity ($z' = z - vt$). The explicit derivation for ρ_r is extensive and will not be
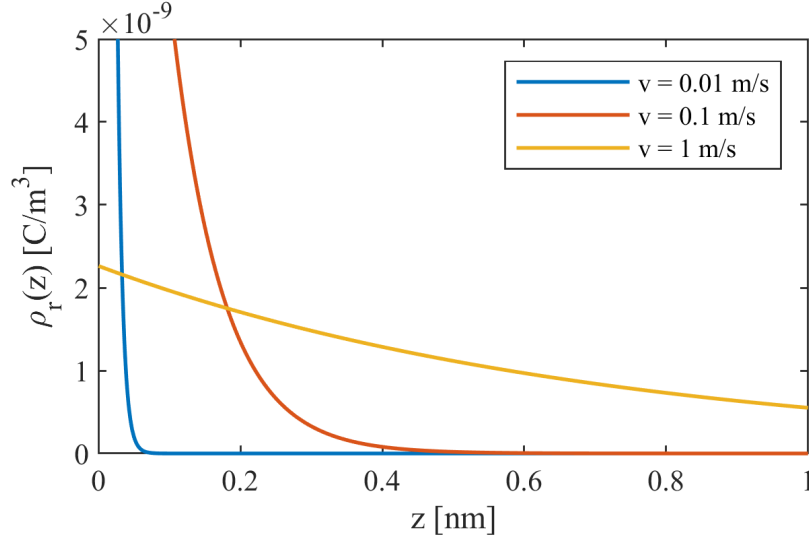
Figure 4.1: Response charge density profile for a moving charge for different velocities as given by Eq. 4.9. The source charge is $q = 10q_e$. The permittivity of the medium is $\varepsilon = 80\varepsilon_0$ and the conductivity is $\sigma = 1\,\mathrm{S/m}$.

reproduced here but can be found in Kalafus's doctoral thesis [92].

$$\rho_r(z') = -\frac{\sigma}{\varepsilon v} \int_0^\infty \exp\left(-\frac{\sigma\zeta}{\varepsilon v}\right) \rho_s(z' - \zeta) d\zeta \tag{4.8}$$

Note that Kalafus was interested in Cerenkov radiation in conductive media and therefore paid special attention to relativistic terms that do not concern us. We assume all velocities are much less than the speed of light ($v \ll c$).

For the case of a point charge at the origin, $\rho_s = q\delta(x)\delta(y)\delta(z)$ where $\delta(*)$ is the Dirac delta function. Substituting this into Eq. 4.8, we obtain:

$$\rho_r(z') = -\frac{\sigma q}{\varepsilon v} \exp\left(-\frac{\sigma z'}{\varepsilon v}\right) \delta(x)\delta(y)u(z') \tag{4.9}$$

Where $u(*)$ is the Heaviside step function. Equation 4.9 allows us to visualize the response charge density of a moving charge as an oppositely charged wake which decays exponentially. The length of this wake is a function of velocity and the properties of the medium. Physically, this can
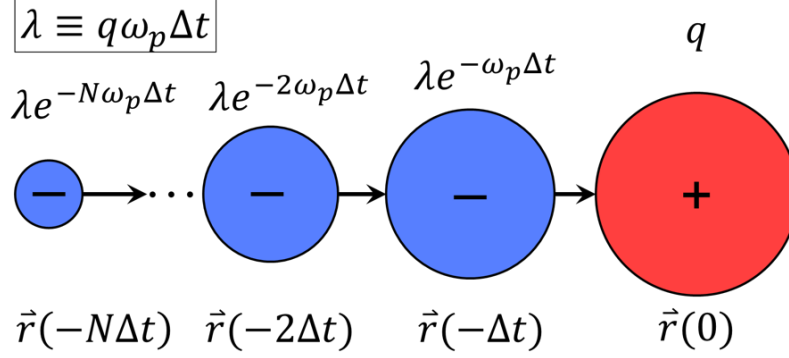
Figure 4.2: Illustration of our virtual charge method. The primary charge (in this case, the red positive charge) moves throughout space as a function of time. Virtual negative charges (blue charges) are placed where the positive charge used to be in previous time steps (assumes continuous knowledge of primary charge's location, interpolation can be used if the primary charge location is only known for discrete time points). The magnitude of virtual charges decays as a function of time, replicating the charge wake.

be interpreted as the counter-ion cloud decaying in the space where the charge used to be. If the charge is moving faster than the relaxation time constant of the medium, the counter-ion cloud will take time to decay at the point where the charge once was. This effect is plotted illustratively in Fig. 4.1.

4.2 Numerical Representation of the Ionic Wake

The response charge density function defined in Eq. 4.9 is still only valid for steady state solutions. To be useful in a BD simulation, we need to account for arbitrary trajectories. Our goal is to come up with a discrete series of point charges that will account for the response charge density of the ionic wake. We pick these charges based on the equivalent Riemann sum of the integral of Eq. 4.9. Integrating Eq. 4.9 over all space yields

$$\int_0^\infty -q\frac{\omega_p}{v}\exp\left(-z\frac{\omega_p}{v}\right)\mathrm{d}z = -q \tag{4.10}$$

where ω_p is the plasma frequency of the medium given by $\omega_p = \sigma/\varepsilon$. This is an intuitive result since the response charge should equal the magnitude of the source. If the source is stationary, the response and source charge would occupy the same space and no fields would exist, as expected for DC fields in conductive medium.

By replacing z with vt we can come up with a Riemann sum to approximate Eq. 4.9.

$$\int_0^\infty -q\frac{\omega_p}{v}\exp\left(-z\frac{\omega_p}{v}\right)dz \approx -\sum_{n=0}^{N} q\omega_p e^{n\Delta t\omega_p}\Delta t \tag{4.11}$$

Where N is the number of "virtual charges" used to represent the ionic wake and Δt is the time step in-between each virtual charge snapshot. In order to represent the ionic wake with a discrete series of charges, we must know the location and magnitude of each point charge. The location is given by the path of the primary charge. Equation 4.11 tells us the magnitude is given by the time past since the source charge was at that location. A diagram illustrating these charges is given in Fig. 4.2.

The error in the approximation will go to zero as N approaches infinity and Δt approaches zero. Practically, it is not necessary to sum infinite charges. We see the magnitude of the response charges decays with an exponential decay constant ω_p. This means we can get a high degree of accuracy if we sum out to the first several decay constants. We define $\tau_p = 1/\omega_p$ and N_τ as the number of time constants to sum. Therefore, the time step in Eq. 4.10 is given by $\Delta t = N_\tau\tau_p/N$. If we define the number of virtual charges and the number of time constants to sum to, Eq. 4.10 can then be defined entirely by the source and media properties. Note that the magnitude of the virtual charges should be adjusted slightly to enforce the response and source charge having the same magnitude and opposite sign.

4.3 Comparison to a Dipole in Conductive Media

To validate our model against the macroscopic case, we can compare to the known case of a dipole in conductive medium. The complex valued electric field for a charge dipole with moment p aligned on the z axis embedded in conductive medium with permittivity ε and conductivity σ is given by [93]:

$$\vec{E} = \frac{p}{4\pi r^3(\varepsilon - i\sigma/\omega)} \left(2\hat{r}\cos\theta - \hat{\theta}\sin\theta\right) \tag{4.12}$$

where ω is the angular frequency of the dipole oscillation.

We simulate a case where a single charge (one electron with $q_e = 1.602 \times 10^{-19}$ C) moves up and down along the z axis with an amplitude (A) of 1 nm. The effective dipole moment is therefore given by $p = q_e A$. The permittivity of the medium is $\varepsilon = 80\varepsilon_0$ and the conductivity is $\sigma = 1$ S/m. In our simulation, $N_{tau} = 5$ and $N = 50$. The electric field strength is measured along the x axis, orthogonal to the axis of the dipole.

Our virtual charge method is compared to the known dipole solution in Fig. 4.3. We see that error between the two is relatively small over a large range of distances and frequencies, suggesting the virtual charge method is robust across many scales.

4.4 Scope of Electrodynamic Interactions

We know that at sufficiently high frequencies, endogenous fields can overcome the plasma frequency and become long range. The derivation from the previous section suggests for transient simulations, we can describe this not just in terms of frequency, but in terms of velocity. This is indeed a more general way of thinking about super-plasma frequency interactions. Even if a dipole is oscillating at a high enough frequency, if the dipole moment is so small because the cycle time is so short, the source will still be weak even if it is "long range". In this section, we will attempt to roughly define the scope of electrodynamic interactions.
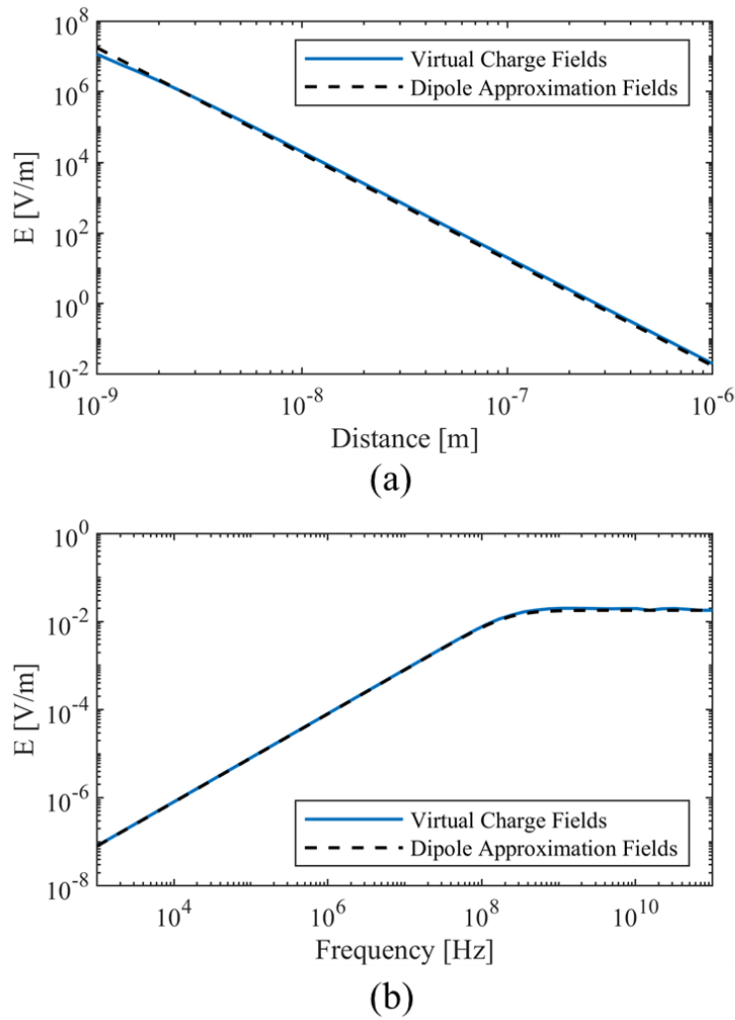
Figure 4.3: Comparison of peak electric field magnitude generated from our virtual charge method with the expectation for a point dipole in conductive medium. (a) Electric field as a function of distance. The frequency used is 1 GHz). (b) Electric field as a function of frequency. The distance used 1 μm. All distances are along the *x* axis, and the dipole is aligned on the *z* axis.

.

To get an estimate of how quickly molecules must be moving for this electrodynamic interaction to be significant, we can simplify our previous expression for a moving charge into a dipole. Consider the wake defined by Eq. 4.9. Since we know total charge of the wake is equal in magnitude and opposite in sign to the primary moving charge, we can define this as an effective

dipole. The length of the dipole is given therefore by the centroid of the wake.

$$l_{eff} = \frac{\int_0^\infty \zeta \rho_r(\zeta) d\zeta}{\int_0^\infty \rho_r(\zeta) d\zeta} = \frac{\varepsilon v}{\sigma} \tag{4.13}$$

$$p_{eff} = q l_{eff} = \frac{q \varepsilon v}{\sigma} \tag{4.14}$$

Using this simple expression for the effective dipole of a moving charge in conductive media, we can determine as a function of distance when such a moving charge could have significant interaction energy with a neighboring charge. It is assumes both charges are of the same magnitude. We define the interaction energy in Eq. 4.15.

$$U = \phi_{eff} q = \frac{p_{eff} q}{4\pi \varepsilon r^2} = \frac{v q^2}{4\pi \sigma r^2} \tag{4.15}$$

Setting this equal to thermal energy, we can solve for the minimum velocity for these charges to have significant EM interaction.

$$v_{min} = \frac{4\pi \sigma r^2 k_B T}{q^2} \tag{4.16}$$

We can also then solve for what strength of driving E field would be required to get the charge to such a velocity in the first place (ignoring inertial terms, which is typically safe in this overdamped environment).

$$E_{min} = \frac{6\pi \eta a v_{min}}{q} \tag{4.17}$$

We use these expressions to analyze two biomolecules. We analyze the DNA base pair, which has a net two electron charge and approximately a 0.3 nm, and tubulin, which has a net 10 electron charge and approximately a 8 nm diameter. The minimum velocity and driving E field are plotted in Fig. 4.4.

We see the velocities necessary for significant electrodynamic interaction are relatively high. Moreover, the electric fields required to drive ions and biomolecules to such velocities are
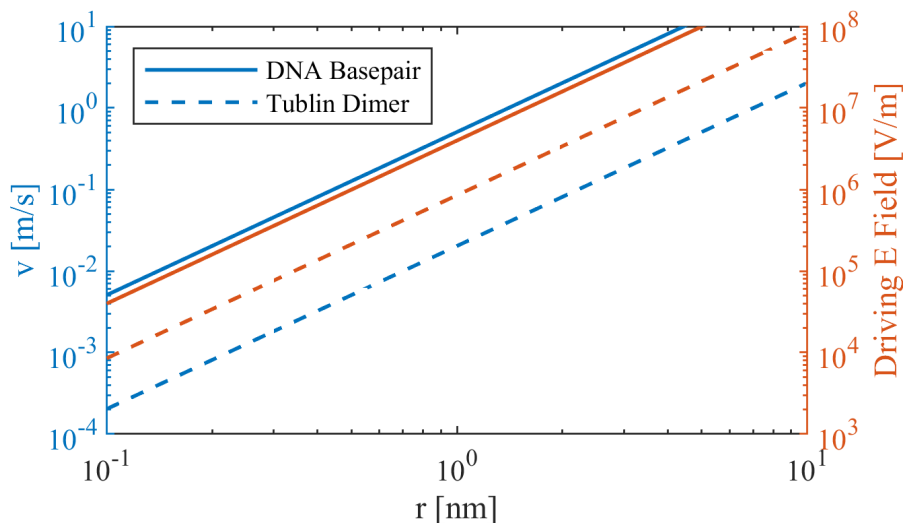
Figure 4.4: Required velocity (left) and the driving electric field required to maintain that velocity (right) as a function of interaction distance for two different biomolecules. Solid lines represent a DNA basepair (net two electron charge and approximately a 0.3 nm) and dashed lines represent tubulin (net 10 electron charge and approximately a 8 nm diameter).

so high they approach dielectric breakdown. Clearly this is not a relevant field strength for those studying weak, non-thermal EM effects. It is more likely such velocities would be achieved by mechanical means. Nevertheless, we will demonstrate what it would take to integrate this virtual charge method into relevant biological simulation techniques.

4.5 Implementation in DNA Model

Our previous work in Chapter 2 suggested the most relevant length scale for biological resonators is on the order of 10 nm to 100 nm. Other than microtubules, chromatin fiber is another promising structure for non thermal EM interaction. To see the effects of our virtual charge method, we implemented an existing coarse grained model of linear DNA. DNA is a negatively charged biomolecule, and therefore one more likely to be electrically active. Coarse grained Brownian dynamics models of DNA are a popular way to study the dynamics of these biomolecules in various conditions [94, 95]. We implement a DNA model first described by [96].

We created a custom Brownian Dynamics simulation that implemented our electrodynamic forces and observed the effects of high field pulses on DNA.

4.5.1 Rod and Bead Model of DNA

Instead of modeling every atom in the DNA molecule, coarse grained models are used to result in the same mechanical properties with much fewer degrees of freedom. Here we reproduce and describe a DNA model implemented first by Jian et. al. [96]. The model is referred to as a "rod and bead" type model because it consists of charged masses connected by springs. Each mass experiences a bending, stretching, and electrostatic force, as depicted in Fig 4.5.
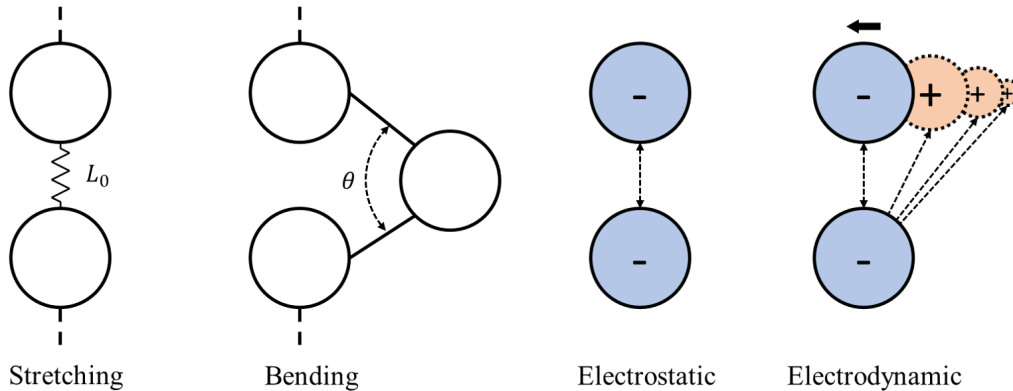
Figure 4.5: Diagram illustrating the different forces the DNA beads experience in our rod and bead model. Beads will be subject to stretching, bending, electrostatic, and electrodynamic forces.

.

The stretching force is essentially a linear spring constant between adjacent beads. Let $\mathbf{r_i}$ be the vector difference bead i and $i+1$, r_i is the magnitude of that vector, and the unit vector $\mathbf{u_i} = \mathbf{r_i}/r_i$. There are N total beads. The stretching force on bead i is given by Eq. 4.18.

$$\mathbf{F^i_{stretching}} = -\frac{h}{2}\left[(r_i - L_0)\,\mathbf{u_i} + (r_{i-1} - L_0)\,\mathbf{u_{i-1}}\right] \tag{4.18}$$

Where L_0 is the natural, unstretched bond length between beads and h is the stretching force

constant. When $i = 1$ or $i = N$, the unit vector towards the non-existent bead can be assumed to be zero.

The bending force is derived from the persistence length of the polymer and represents its ability to resist sharp bending. While the bending energy is simple to calculate, explicit expressions are more complicated. We use explicit equations derived by Allison et. al. in Eq 4.19 [97].

$$\mathbf{F}^{\mathbf{1}}_{\mathbf{bending}} = -g(\mathbf{u_2} - \mathbf{u_1})/r_1$$

$$\mathbf{F}^{\mathbf{2}}_{\mathbf{bending}} = -g(\mathbf{u_2} - \mathbf{u_1})(1/r_1 + 1/r_2) - g(\mathbf{u_3} - \mathbf{u_2})/r_2$$

$$\mathbf{F}^{\mathbf{i}}_{\mathbf{bending}} = -g(\mathbf{u_{i-1}} - \mathbf{u_{i-2}})/r_{i-1} - g(\mathbf{u_i} - \mathbf{u_{i-1}})(1/r_{i-1} + 1/r_i) - g(\mathbf{u_{i+1}} - \mathbf{u_i})/r_i \quad (4.19)$$

$$\mathbf{F}^{\mathbf{N-1}}_{\mathbf{bending}} = -g(\mathbf{u_{N-2}} - \mathbf{u_{N-3}})/r_{N-2} - g(\mathbf{u_{N-1}} - \mathbf{u_{N-2}})(1/r_{N-2} + 1/r_{N-1})$$

$$\mathbf{F}^{\mathbf{N}}_{\mathbf{bending}} = -g(\mathbf{u_{N-1}} - \mathbf{u_{N-1}})/r_{N-1}$$

Where g is the bending rigidity constant. The middle equation is valid for $3 \leq i \leq N - 2$.

The electrostatic force represents electrostatic repulsion between the charged body. These interactions are subject to screening and decay exponentially with the Debye length, as described in chapter 2. In this expression, we take r_{ij} to be the vector position difference between bead i and bead j, r_{ij} is the magnitude of that vector, and the unit vector $\mathbf{u_{ij}} = \mathbf{r_{ij}}/r_{ij}$.

$$\mathbf{F}^{\mathbf{i}}_{\mathbf{electrostatic}} = \sum_{j \neq i}^{N} \frac{q_i q_j}{4\pi\varepsilon r_{ij}^2} e^{-r_{ij}/\lambda_D} \mathbf{u_{ij}} \quad (4.20)$$

Where ε is the permittivity of the medium, λ_D is the Debye length, and the charges q_i and q_j are each given by νL_0, where ν is the linear charge density of DNA. We see this expression requires a sum across every bead, meaning this will contribute more to computational complexity as the structure scales.

Finally, in addition to the three forces described in the original work, we also compute our electrodynamic force. The electrodynamic force is computed exactly the same as the electro-

Table 4.1: Parameters used for DNA simulation.

Variable	Description	Value	Units
L_0	Unstretched length between beads	5	nm
h	Stretching force constant	$100 k_B T / L_0^2$	J/m^2
g	Bending rigidity constant	$9.82 k_B T$	J/rad^2
ν	Effective linear charge density	0.243	electron/Å
a	Bead radius	1.59	nm
T	Temperature	298	K
ε_r	Relative permittivity of medium	80	N/A
σ	Conductivity of medium	1	S/m
η	Viscosity of medium	8.9×10^{-4}	Pa s

dynamic force, except without the exponential decay term of Debye screening. For every primary charge, the force is computed with every other primary charge and their virtual charges. A primary charge does not experience a force from its own virtual charges, and the virtual charges themselves do not experience forces. This assumes that the viscosity any primary charge experiences will be a much greater damping force than the drag from its own virtual charge wake. It also assumes virtual charges will dissipate quickly enough that we can ignore forces acting on them. This assumption may not always be accurate, but as the magnitude of the electrodynamic force should overall be small, it should provide reasonable outcomes.

4.5.2 Brownian Dynamics Simulation

Brownian dynamics is a simulation technique for modeling the interactions of many bodies in a thermal environment with random Brownian motion. It is a simplified version of Langevin dynamics, where the mass is assumed to be very small and inertial terms are ignored. Brownian dynamics can be a much more computationally efficient than AA-MD because the solvent is not simulated explicitly. Instead the interactions with the solvent are accounted for using continuum parameters and statistical mechanics.

The most common, first order equation for generating the new position vector is given in

Eq. 4.21 [98].

$$\mathbf{x_{n+1}} = \mathbf{x_n} + \frac{\Delta t}{k_B T} \mathbf{D_n} \cdot \mathbf{F_n} + \mathbf{R_n} \tag{4.21}$$

Where $\mathbf{x_n}$ is the position vector at time step n, Δt is the time step, $\mathbf{D_n}$ is the translational diffusion tensor, $\mathbf{F_n}$ is the sum of all forces acting on the $\mathbf{R_n}$ is a random displacement generated at each time step.

The translational diffusion tensor is a 3 by 3 matrix for every bead combination. It represents hydrodynamic interactions between beads, a force which has been shown to be significant [98]. It also introduces viscosity and creates drag. For $i \neq j$, the translational diffusion tensor is given by Eq. 4.22, and by Eq. 4.23 for $i = j$.

$$\mathbf{D_{ij}} = \frac{k_B T}{8\pi\eta r_{ij}} \left[\left(\mathbf{I_3} + \frac{\mathbf{r_{ij}r_{ji}}}{r_{ij}^2} \right) + \frac{2a^2}{r_{ij}^2} \left(\frac{1}{3}\mathbf{I_3} - \frac{\mathbf{r_{ij}r_{ji}}}{r_{ij}^2} \right) \right] \tag{4.22}$$

$$\mathbf{D_{ii}} = \frac{k_B T}{6\pi\eta a} \mathbf{I_3} \tag{4.23}$$

Where $\mathbf{I_3}$ is a 3 by 3 identity matrix and η is the viscosity of the medium. The random displacement is given by Eq. 4.24.

$$\mathbf{R} = \mathbf{G} \sqrt{\Delta t \frac{k_B T}{6\pi\eta a}} \tag{4.24}$$

Where $\mathbf{G}$ is a vector of three random values normally distributed with mean zero and standard deviation of one. This means $\mathbf{R}$ is normally distributed with mean zero and variance of $\frac{k_B T}{6\pi\eta a}\Delta t$.

4.6 External Electric Field Impact on Linear DNA Strand

The Brownian dynamics code and DNA model, along with the virtual charge algorithm, was implemented in MATLAB. We simulated a DNA model with 41 beads, corresponding to approximately 600 basepairs. Each trial was simulated with a timestep of 100 ps for a duration of 10 ns. A total of 5 virtual charges were used out to 3 total plasma time constants. We simulated

the DNA strand when exposed to an electric field step function starting at 5 ns. The strength of the electric field step function was varied. Each electric field strength was simulated with five independent trials to account for the stochastic nature of the simulation. Each trial had the same starting position, which was obtained by running a 10 μs with no external field to determine a typical rest DNA.

A common measure of DNA polymer dynamics is the end to end distance, which is the distance between either end of DNA. This can be thought of as a metric of how compact the DNA strand is. The end to end distance for every trial is shown in Fig. 4.6. As predicted in
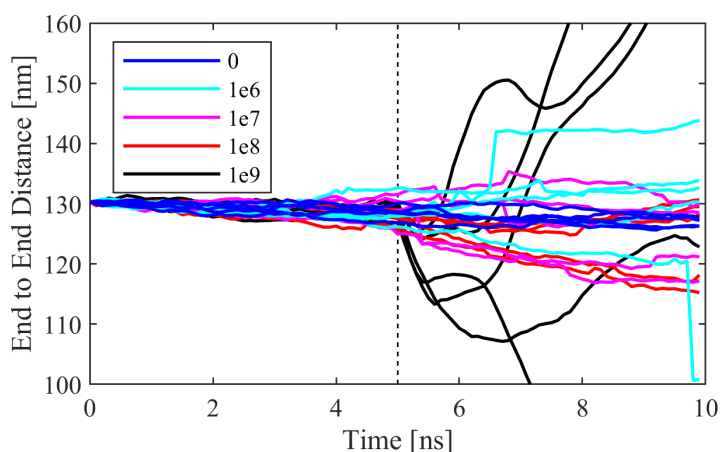
Figure 4.6: End to end distance of linear DNA strand after being subjected to an electric field step function that turns on at 5 ns (indicated with the dotted black line). The legend corresponds to the magnitude of the field pulse in V/m. Each magnitude case was ran five independent times to help account for averaging. We see that as the E field strength increases, the end to end distance deviates more over time, suggesting that the field pulse can induce significant contraction or repulsion depending on the starting position of the DNA.

.

the previous section, extremely high field strengths are necessary to drive the DNA beads at velocities sufficient to make the electrodynamic force competitive with other forces. At higher field strengths, the DNA strand end to end distance begins rapidly increasing or decreasing.

63

4.7   Conclusions

In this chapter we discussed why the treatment of electrodynamic interactions in conductive media with transient simulations is a difficult problem. Based on theory from Cerenkov radiation in conductive media, we presented an analytic formulation for the "counter-ion wake" left behind by moving charges. In order to extend this to numerical simulations, we presented a technique that takes the Riemann sum of the charge wake with a discrete number of "virtual charges". We found this agreed well with the expected macroscopic results. Upon closer examination, we determined such electrodynamic forces would only be significant when moving charges achieved relatively high velocities, which would require some external forcing or very high electric fields. Finally, we implemented a rod and bead model of DNA and confirmed that extremely high electric fields were required to perturb the system.

This concludes our modeling efforts in this thesis. The next chapter will cover our experimental work, in which we attempt to provide direct and indirect evidence of biological signaling using EM fields.

This chapter is based on "Modeling Electrodynamic Interactions in Brownian Dynamics Simulations" by KA Thackston, M. Casebeer, DD Deheyn, DF Sievenpiper. *In preparation.* The dissertation author was the primary author of this material.

Chapter 5

Experimental Methods

In addition to our computational modeling, we also performed experiments attempt to measure evidence of EM signaling in cells. Broadly speaking, these experiments can be categorized into three types as shown in Fig. 5.1: listening experiments (where we attempt to measure a signal directly), stimulating experiments (where an external signal is applied in the hopes of observing a change in biological function), and indirect experiments (where some part of the environment is changed that should impact EM signaling, and we observe for change of biological function). Here I discuss our experimental methods of our listening and indirect experiments. While stimulating type experiments were also performed, no positive effect was identified.

Listening experiments have the advantage of providing some of the most compelling evidence for biological signaling. The challenge, however, is measuring extremely weak EM fields of unknown frequency or polarization. In any signal measurement, noise will increase proportionally with bandwidth. The frequency of any biological EM signaling, however, is completely unknown. Measuring such a large spectrum with a narrow bandwidth measurement is not practical. This is the key challenge of direct listening experiments, along with other difficulties of weak signal detection [99].
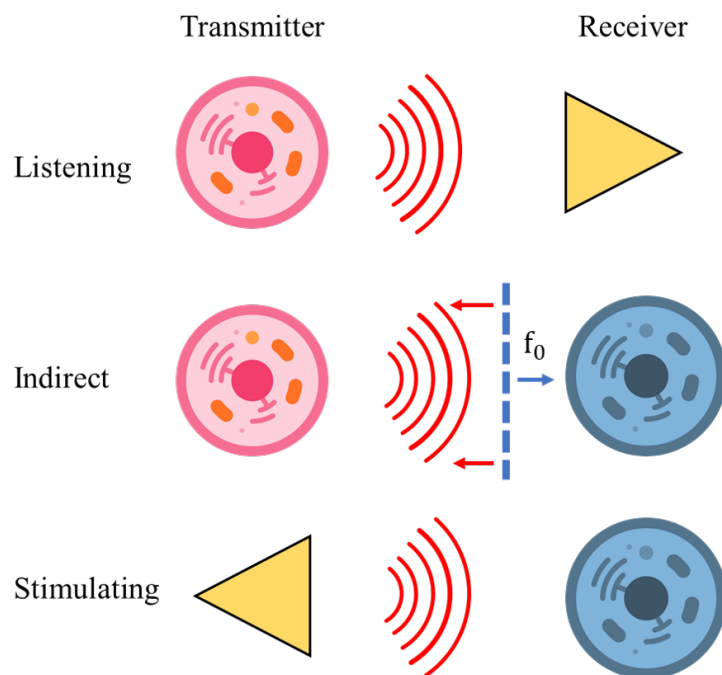
Figure 5.1: The attenuation of our aluminum box chamber. Transmission here was measured by using a network analyzer to measure S21 between the two the ports located on the edge of the aluminum chamber. Attenuation here is defined as the difference in transmission between the normal arrangement of the chamber, and when the top half of the chamber is inverted, thus placing the aluminum layer in between the two probes. The attenuation is greater than 30 dB for all measured frequencies.

The most common type of indirect experiment is the barrier experiment. Two biological samples are separated in containers that ideally are chemically distinct. Between the two samples, some sort of EM barrier is placed. The experimenter then observes if there is any difference in biological activity depending on the type of barrier placed. As described in Section 1.1.1, Alexander Gurwitsch originally performed this type of experiment with his onion roots as biological samples, and the activity he observed was an increase in mitosis. Because he used glass and quartz barriers and observed the increase for quartz but not glass, he inferred hypothetical the signal was in the UV spectrum. Many variation of barrier experiments have since been performed [5] with little variation to the original experimental design, and have not produced overwhelming results.

At its core, the barrier experiment is an attempt to interfere with an unknown communica-

RF Absorber to cancel out cavity resonances

Conductive mesh
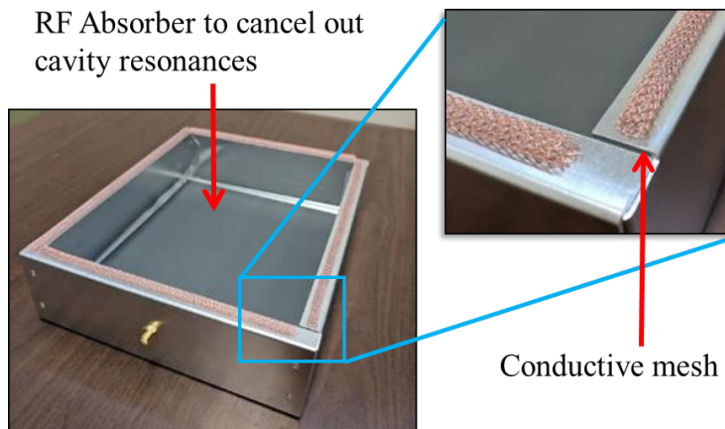
Figure 5.2: Picture of one half the Faraday chamber.

tion channel. This is considered advantageous because of the difficulties of direct measurement compared to measuring change in biological activity. The barrier is essentially acting as a filter. We propose a more advanced version of the barrier experiment where a set of frequency selective surfaces (FSS) will be used in lieu of glass or quartz in order to investigate a lower bandwidth with much greater resolution.

5.1 Faraday Cage Chambers

To mitigate external EM signals as a confounding factor in our experiments, we devised Faraday cage testing chambers to perform our experiments in. Our chambers consist of two aluminum boxes with open tops (10" x 8" x 2.5", 1 mm thick). Inside each chamber is a 1 mm thick absorber sheet to prevent cavity resonances (MAST Technologies high loss cavity resonance absorber MR42-0007-20). The rims of the aluminum boxes are lined with conductive mesh gasket to provide a conductive seal when the chambers are closed. Through-hole coax connectors allow us to connect devices between the inside and outside of the chamber. A picture of one half the chamber is shown in Fig. 5.2.

To confirm these chambers could function as reasonable Faraday cages, we measured the attenuation of the chamber as described in Fig. 5.3, as well as the shielding of the chamber

to external tones as described in Fig. 5.4. The attenuation of our chamber was measured with a two port Keysight Network Analyzer (model E5071C, 300 kHz – 20 GHz). For the shielding measurement, the feed was connected to two cascaded amplifiers (both RF Lambda© RLNA00M65GA yielding a total maximum of 80 dB of gain over 0.03 GHz to 65 GHz). The output of the amplifier was fed into a spectrum analyzer (Keysight© 50 GHz FieldFox Microwave Spectrum Analyzer).
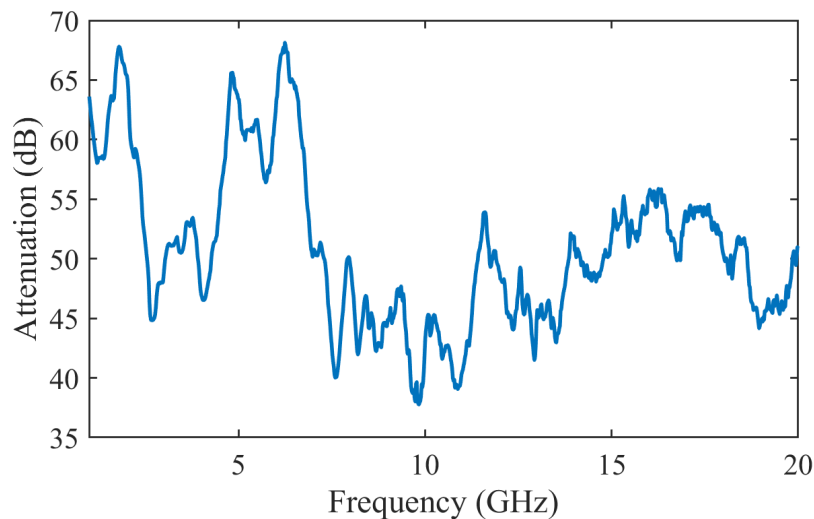
Figure 5.3: The attenuation of our aluminum box chamber. Transmission here was measured by using a network analyzer to measure S21 between the two the ports located on the edge of the aluminum chamber. Attenuation here is defined as the difference in transmission between the normal arrangement of the chamber, and when the top half of the chamber is inverted, thus placing the aluminum layer in between the two probes. The attenuation is greater than 30 dB for all measured frequencies.

5.2 Frequency Selective Surface Design

Instead of using glass or quartz barriers, we design more advanced and tailored EM filters for our barrier experiments. A Frequency Selective Surface (FSS) is a type of metasurface that acts like a filter for an incoming EM plane wave, allowing certain frequencies to pass and reflecting others [100].
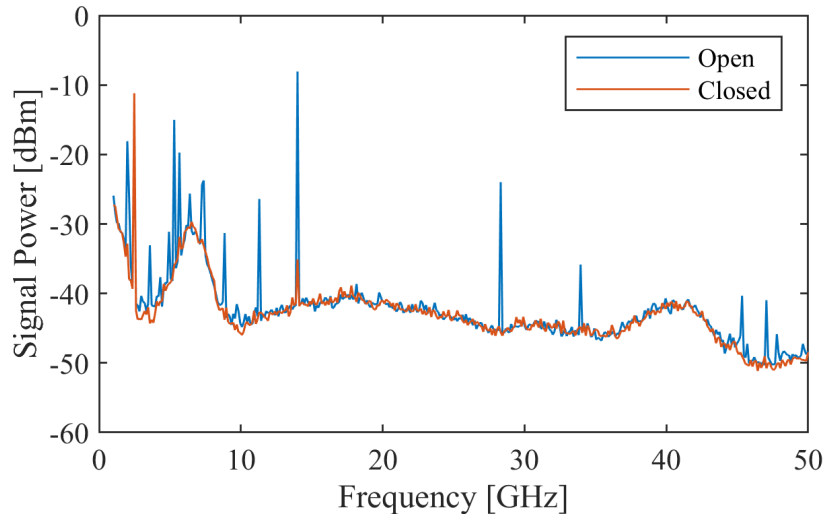
Figure 5.4: Demonstration of the chamber's ability to shield from external signals. Measurement was done by plugging into the chamber's feed with and without the lid on. Many tones which appear in the open case are removed when the chamber is closed. The feed was connected to two cascaded amplifiers (both RF Lambda© RLNA00M65GA yielding a total maximum of 80 dB of gain over 0.03 GHz to 65 GHz). The output of the amplifier was fed into a spectrum analyzer (Keysight© 50 GHz FieldFox Microwave Spectrum Analyzer).

Typically an FSS will be designed with resonant structures in the unit cell, such as a Jerusalem cross or large dipole slots. For our application, we use a Miniaturized Element Frequency Selective Surface (MEFSS). This metasurface consists of repeated capacitive metal patch layers and inductive metal grid layers, as opposed to a single resonant feature like a Jerusalem cross. By tuning the inductance and capacitance of each layer, one can design a desired filter response, giving us a much greater degree of control over our experiment than previous barrier experiments. By overlapping two capacitive sheets closely, we can decrease the entire unit cell of the system, which increases robustness to angle of incidence and polarization and shifts up the second harmonic. The unit cell of our MEFSS design is shown in Fig. 5.5.

The design theory for our MEFSS can be found in [101]. Although the cited work provides a synthesis method for the FSS, we found the method insufficient to design a filter to our desired tolerances. The previously published synthesis method claims to find initial values for the filter geometry that can be tuned to get the desired response. However, we found the initial values so

69
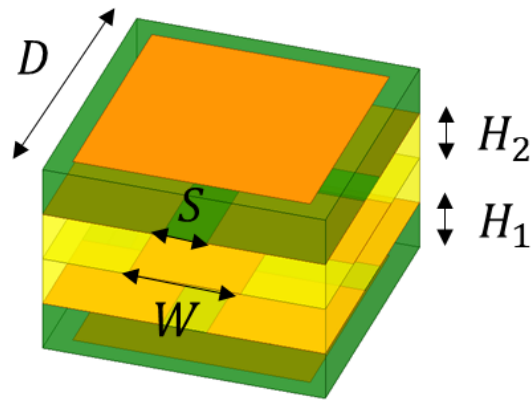
Figure 5.5: Diagram of FSS filter design. The FSS is defined by the periodicity of the unit cell (D) the gap between capacitive patches (S), the width of the inductive grids (W), the thickness of the outer substrate layers (H1) and the thickness of the inner substrate layers (H2). All substrates are the same dielectric (Rogers 4350b).

far from the proper geometry that brute force optimization was a more efficient design method. We designed six filter frequency responses to span the bandwidth of $10\,\text{GHz}$ to $60\,\text{GHz}$. The polynomial representation of these filters was imported into Ansys HFSS. Each FSS was designed by using the HFSS optimization tool to minimize the R^2 value between the actual and desired filter response. The design variables used were D, S, and W as depicted in Fig. 5.5. The thicknesses of the substrates were chosen based on commercial thicknesses available.

This class of FSS has three main advantages. First, the filter response is robust over many angles of incidence and polarizations, which is necessary for our experiment as we cannot assume the fields generated by the cell cultures form an oncoming plane wave. Moreover, the filter response is even robust to near fields, as shown in our simulation in Fig. 5.6. Second, unlike many FSS designs, this MEFSS has a suppressed second harmonic, allowing us to design multiple independent filters over a large bandwidth. Third, the design is extremely thin; our lowest frequency filter has thickness of less than $\lambda/20$. This allows us to keep the cells close enough for interaction, as our experiments suggest any signaling effect drops off after 5 mm, as shown later in Fig. 5.11.

The first five filters consist of five total layers: two capacitive patch layers, followed by an
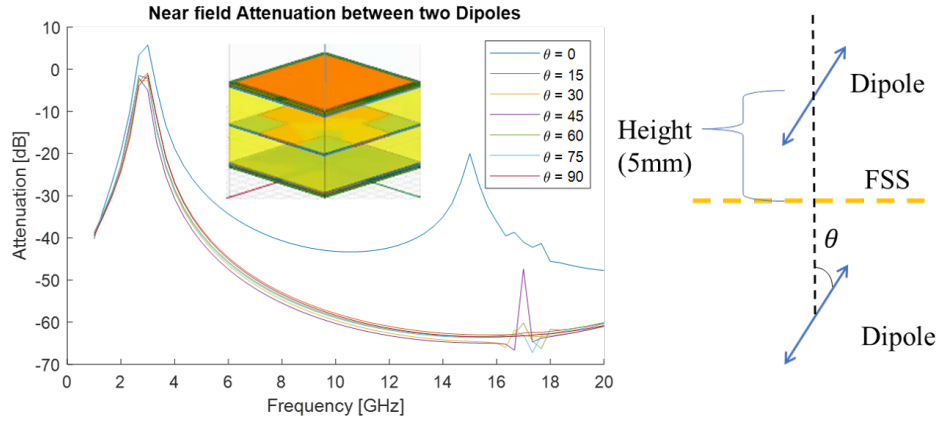
Figure 5.6: Simulation of the near field attenuation of the MEFSS design in HFSS. Two dipole sources were placed 5 mm above and below the FSS. Attenuation is defined as the difference in transmission with and without the FSS. The dipole sources are rotated in 15 degree increments to change the vector alignment of the electric field (i.e. when $\theta = 0$ degrees, the E field is normal to the FSS, and when $\theta = 90$ degrees, the E field is tangent to the FSS). We see the bandpass filter response is extremely robust for different angles, suggesting the FSS will still perform as expected during biological experiments where the vector orientation of the signal cannot be assumed. The apparent gain occurring for $\theta = 0$ degrees is likely because of the resonance of the FSS increasing the near field coupling.

inductive grid, followed by two more capacitive patch layers. The sixth is a three layer design which goes patch-grid-patch. The geometry of every filter is given in Table **??**. All filters use Rogers 4350b as the substrate, with a relative permittivity of 3.66.

The transmission of the filters was measured with two WR62 horn antennas and a two port Keysight Network Analyzer (model E8361A, 10 MHz – 67 GHz). All simulations were performed in Ansys HFSS. We see that the FSS filter response is close to simulated design for most cases, though the highest frequency case seems to have significant deviation. It is possible

Table 5.1: Geometric values for all six FSS filters used.

Filter	f_0	D (mm)	W (mm)	H1 (mm)	H2 (mm)	S (mil)	Thickness (mm)
1	12	1.423	0.429	0.101	0.422	4	1.046
2	19	1.102	0.341	0.101	0.388	4	0.878
3	28	0.948	0.269	0.168	0.254	4	0.844
4	37	0.950	0.380	0.168	0.168	6	0.672
5	46	0.75	0.330	0.168	0.168	6	0.672
6	59	0.706	0.182	N/A	0.338	8	0.676

this is because that bandwidth is so far from the operating frequency of the horn antennas used.
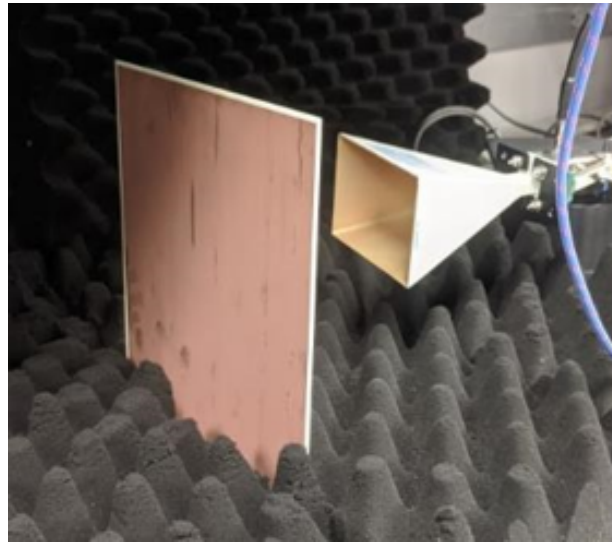
Figure 5.7: Picture of the FSS measurement setup. Two horn antennas were used to measure the transmission of each FSS. Absorption foam on the perimeter of the measurement setup helps reduce side lobes which go around the FSS.
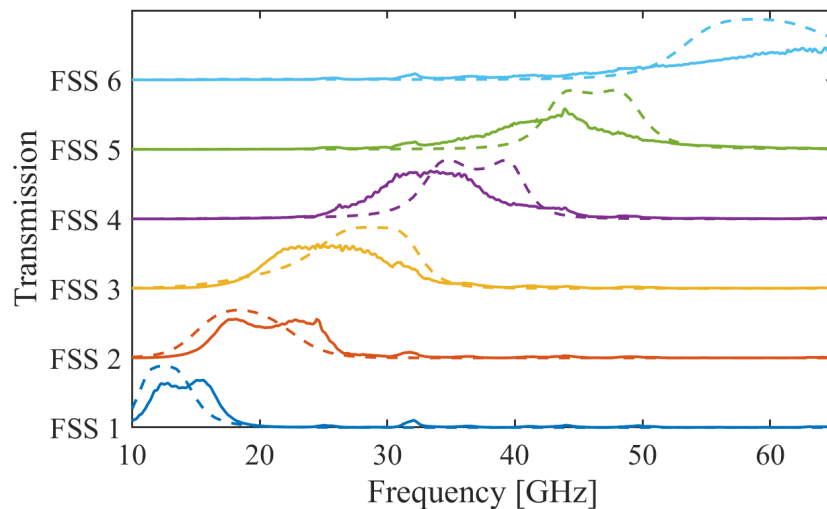
Figure 5.8: The measured (solid lines) vs. simulated (dotted lines) bandpass responses of all six FSS filters. The frequency response is shown here in a linear scale. It is believed that deviations from the simulation for the higher frequency filters stems from the difficulty of measuring transmission at these frequencies using WR62 horn antennas.

5.3 Barrier Experiments

This section performed mainly by our collaborators at the Scripps Institute of Oceanography, but we report their results here. Essentially, two cell cultures are separated in the Faraday cage chambers in separate flasks. When one cell culture is radiated with UV light, evidence of cell stress can be measured using a comet assay. A comet assay is gel electrophoresis method for measuring DNA strand breaks in eukaryotic cells. Negatively charged DNA will diffuse towards the anode, creating a comet tail effect in the gel once the DNA is florescently tagged. The length of the comet tail corresponds to the amount of DNA strand breaks, as small pieces of DNA will diffuse farther. In our experiment, cell cultures will be exposed to UV radiation to induce stress and cause DNA damage, resulting in longer comet tails. Cells not exposed to UV radiation will be termed "naïve". All cell cultures are in sealed $25\,\text{cm}^2$ flasks.

In the experiment, one C3H culture (receiving) is placed next to another isolated C3H culture previously exposed to UV radiation (signaling) in our EM shielding chamber without FSS in between for an hour. As a control, the UV irradiated C3H cells were swapped with naïve C3H cells on the signaling side. The cellular response on the DNA level of the two receiving C3H cultures was later assessed by comet assay. As a result, the olive moment of C3H cells next to UV irradiated cells (positive) is consistently higher than that of C3H cells next to naïve cells (negative) (Fig. 5.10). This suggests that a UV induced, non-chemical signal is transmitted/received between the two cell flasks, and this signal can affect the cellular behavior at the DNA level. A diagram outlining the experiment is shown in Fig. 5.9.

5.3.1 Cellular response is frequency dependent

We repeated the above experiment with the six FSS filters designed to have different passbands in the gigahertz range. Across the six FSS filters that we tested, only FSS3 with a passband of 23 GHz to 32.5 GHz showed the same effect of olive moment elevation as the positive
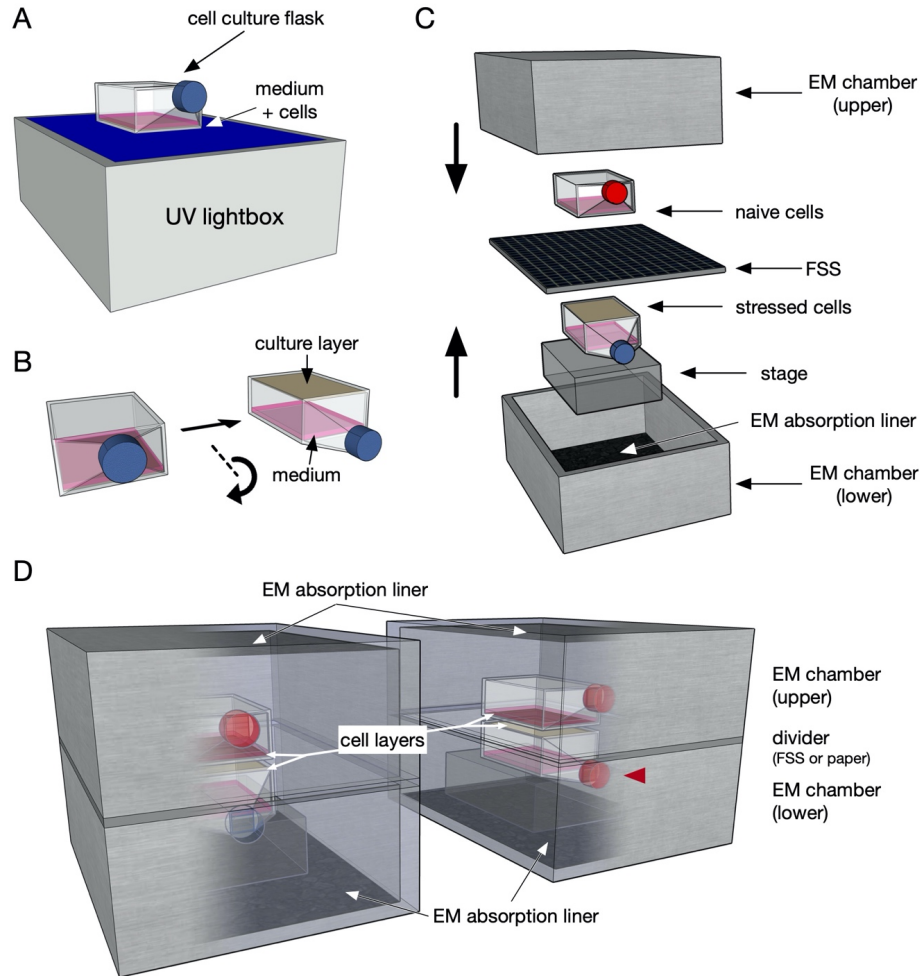
Figure 5.9: Experimental workflow and setups. A) A flask of C3H cell culture (70% confluency) is placed on top of a UV lightbox and then irradiated with $180 \, \text{kJ/m}^2$ of UV radiation at a wavelength of 302 nm. B) The UV irradiated cell culture flask (blue cap) is then inverted. C) After inversion the flask was placed inside the lower half of an experimental EM shielding chamber. Another culture flask with naïve (non radiated) C3H cells (70% confluency, red cap) is placed on top of the irradiated culture flask dividing by a frequency selective surface (FSS) of varies passbands. The irradiated culture flask is elevated by a stage so that the cell attaching surface of each flask is in close contact with the FSS filter. D) Naïve cells (red cap, upper chamber) are housed inside the EM shielding chamber for one hour before disassembled and proceed with comet assay protocol. In the positive control, the FSS filter was replaced by a layer of EM permeable material of the same thickness (i.e. paper). In the negative control, in addition to the EM permeable divider, the culture flask in the lower half of the chamber is replaced by yet another flask with naïve cells (red arrowhead). This figure is reproduced here with permission by its creator, Dr. Bor-Kai Hsiung.

control (i.e. receiving cells next to UV-irradiated signaling cells without FSS, Fig. 5.10). This frequency-dependent olive moment elevation would further suggest the signal is of an EM nature in the gigahertz regime.
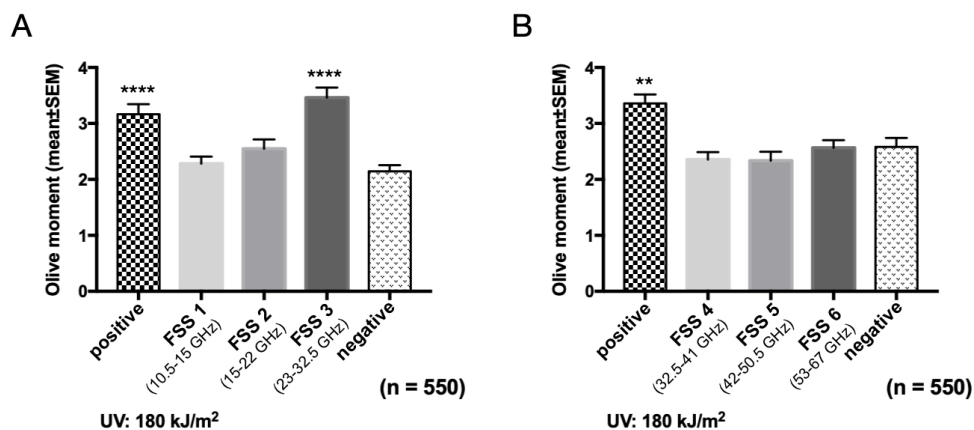
Figure 5.10: A UV-induced, frequency-dependent EM stress signal was observed. The signal likely resides within 23 GHz to 32.5 GHz. A) An elevated olive moment was observed in the naïve cell population spatially adjacent to the UV-irradiated cell population (positive) divided by an EM permeable barrier. The two cell populations are physically separated by individual flasks suggesting that the signal is not transmitted through chemical diffusion. In contrast, the olive moment was not elevated if juxtaposed to another naïve cell population across the divider (negative). FSS with three different passbands (FSS1-3) as the barrier was also tested accordingly. Only FSS3 with 23 GHz to 32.5 GHz passband resulted in the same elevated olive moment as the positive control. B) Again, the olive moment of the positive control was significantly higher than that of the negative control. FSS filters with three more passbands (FSS4-6) were further tested, none of them shown elevated olive moment as the positive control. ** indicates p $\leq$ 0.01, **** indicates p $\leq$ 0.0001. This figure is reproduced here with permission by its creator, Dr. Bor-Kai Hsiung.

5.3.2   Cellular response over distance

In Chapter 2, our calculations suggest that near field interaction is more likely than far field interaction at this gigahertz frequency range. To evaluate the impact of distance, we performed experiments using a modified setup. No FSS was used and the distance between the two cell flasks was varied. As expected, the measured effect decreases as cell cultures are moved farther apart. When the cell layers are separated at 7 mm or more, the olive moment of the receiving

cells returned to an unelevated background level (Fig. 5.11). This result is the primary reason we constrained our FSS filters to be so thin (< 1 mm).
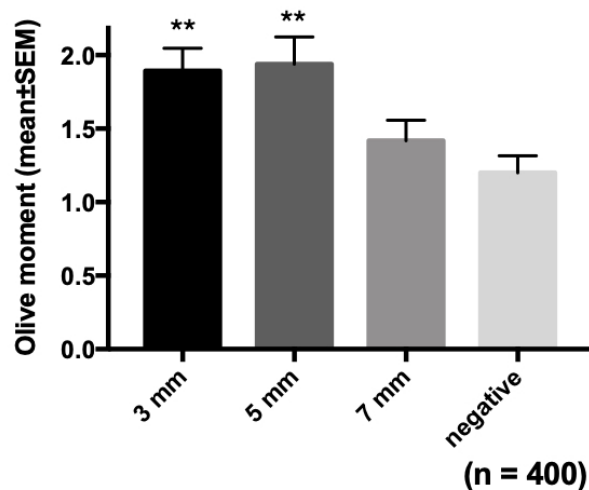
Figure 5.11: The experiment was done according to Fig. 5.9 (180 kJ/m^2 one hour), except we varied the distance between the naïve cell culture and the UV-irradiated cell culture instead of varying the FSS passbands. Significantly elevated olive moment can be observed up to 6 mm (Fig. 5.10, positive) between the two culture flasks, suggesting that the UV-induced EM stress signal can be sensed by C3H cells within 6 mm distance. ** indicates p ≤ 0.01. This figure is reproduced here with permission by its creator, Dr. Bor-Kai Hsiung.

5.3.3 Cellular response over time

The biological response as a function of time was also investigated. We performed a series of experiments using the same setup as the positive control (no FSS), where the only variable is the time duration the two cell layers were put next to each other (as opposed to always one hour). The olive moments of the UV irradiated cells are at their peak roughly between 30 min to 60 min after UV irradiation, then return to the basal level (Fig. 5.12A). The olive moments of the naïve cells generally follow the same trend and mirror that of the UV irradiated cells (Fig. 5.12B), suggesting the cellular signal(s) affecting the naïve cells are indeed induced by UV and are originated from the UV irradiated cells.
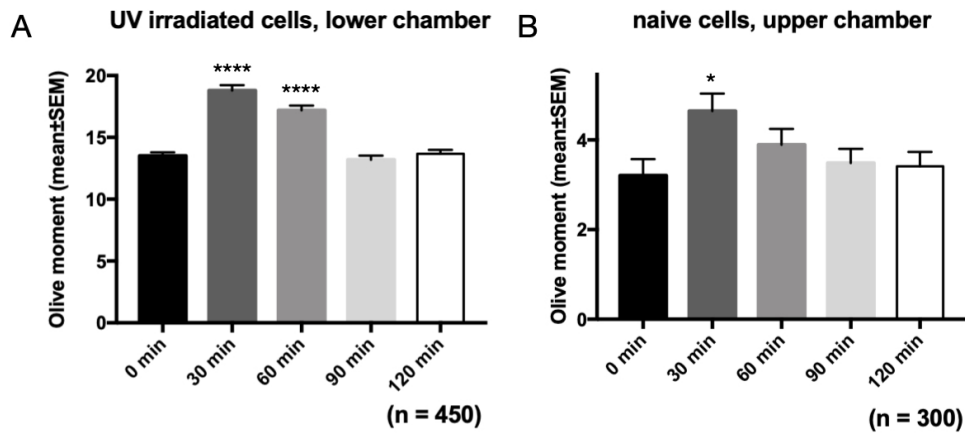
Figure 5.12: The olive moments of naïve cells temporarily mirrored that of the UV-irradiated cells. A UV-irradiated flask was first exposed to $180\,\mathrm{kJ/m^2}$ of UV radiation, then both culture flasks were placed inside the EM-shielding chamber as depicted in Fig. 5.9 for time-dependent endpoint studies without an FSS divider. Comet assays were performed after the designated time to quantify the olive moments for the cells of each flask. A) Significantly elevated olive moments were observed at both 30 min and 60 min time points. B) Elevated olive moments of the naïve cells were also observed at both 30 min and 60 min time points, although only that of the 30 min time point was statistically significant due to small sample size in this particular experiment. The trend of the time dependent olive moments of the naïve cells mirrored that of the UV-irradiated cells, suggesting the naïve cells can sense signals from UV-irradiated cells although being physically separated. Overall, the results suggest there is indeed a UV-induced signal after UV irradiation, and this signal decays after 90 min. * indicates $p \le 0.05$, **** indicates $p \le 0.0001$. This figure is reproduced here with permission by its creator, Dr. Bor-Kai Hsiung.

5.3.4   Summary

The barrier experiments suggest some signaling is occurring between the UV stressed and the non stressed cells. Because the cells are in different flasks, it is unlikely the signal is chemical in nature. Varying the experiment as a function of time shows the effect occurs closely to when the UV radiation occurs, further reinforcing the cellular effect is a result of the UV radiation, and not some other variable. By varying the distance between cell cultures, we obtain evidence the effect is distance dependent, further suggesting that the effect is indeed the result of some cellular signal. Finally, by using the six different FSS filters, we obtain evidence the signal is also frequency dependent, potentially in the bandwidth of $20\,\mathrm{GHz}$ to $30\,\mathrm{GHz}$.

5.4 Cell Listening Experiments

The effect measured in Section 5.3 suggests some signaling could be present at 20 GHz to 30 GHz. The next logical step is to attempt to measure the signal directly. To this end, we performed a variation of the barrier experiments, replacing the FSS filter with a small metal probe that sat in-between the two cell flasks. The probe was fed into low noise, high bandwidth amplifiers, and then into a high bandwidth spectrum analyzer. A single measurement (frequency sweep) was made every 15 minutes for both three different cell cases. A diagram of the experiment is shown in Fig. 5.13.
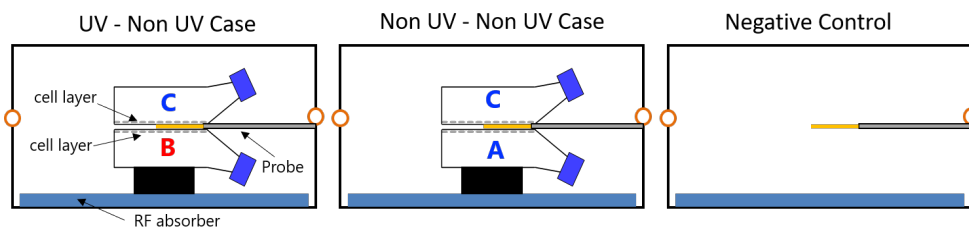
Figure 5.13: Diagram of the listening experiment setup. Cells A and C are the control cells and are never exposed to UV. Cells B are exposed to UV. We measured the flask at 5 intervals: 0, 15, 30, 45, and 60 minutes after UV. At each time interval we measured Cells A, Cells B, and a Control case for all frequency bands. Measurements were done over 1 GHz to 50 GHz, 23 GHz to 32.5 GHz, and 40 GHz to 50 GHz. The resolution bandwidth was 10 kHz.

The spectrum analyzer used was a Keysight N9962A FieldFox Handheld Microwave Spectrum Analyzer (9 kHz - 50 GHz). We used two ultra wide band amplifiers (RF Lambda model RLNA00M65GA) which operated up to 50 GHz and provides 40 to 33 dB of gain. For the sake of time, a 10 kHz resolution bandwidth was used during measurements. The noise floor of such a measurement is calculated using Eq. 5.1.

$$N_{dBm} = 10\log_{10}(1000k_B T) + NF + 10\log_{10}(BW) \tag{5.1}$$

Where N_{dBm} is the noise floor of the measurement, NF is the noise figure of the amplifier chain, and BW is the bandwidth of the measurement. For our measurement, $NF = 5.5$ dB, $BW =$

10 kHz, and $T = 290$ K. The noise floor can then be computed as -128.5 dBm. Quantifying the minimum detectable signal is difficult because we cannot make a good estimate of how well the cell signal would couple into the probe. When performing the experiment, the amplifiers were allowed to warm up for approximately 15 minutes before starting to avoid temperature drift.

Signal power is defined as the difference between the UV radiated cell measurement and the non-UV cell radiated measurement. If the UV radiating cells were emitting some EM signal, we would expect signal power to be positive at some frequency. After running multiple trials, for every bandwidth and time frame, we found no evidence of a positive signal power, even when the control (no cells) was used as a reference. A single instance of this data is shown in Fig. 5.14. For the sake of space, not every instance will be shown in this thesis since all results were negative.
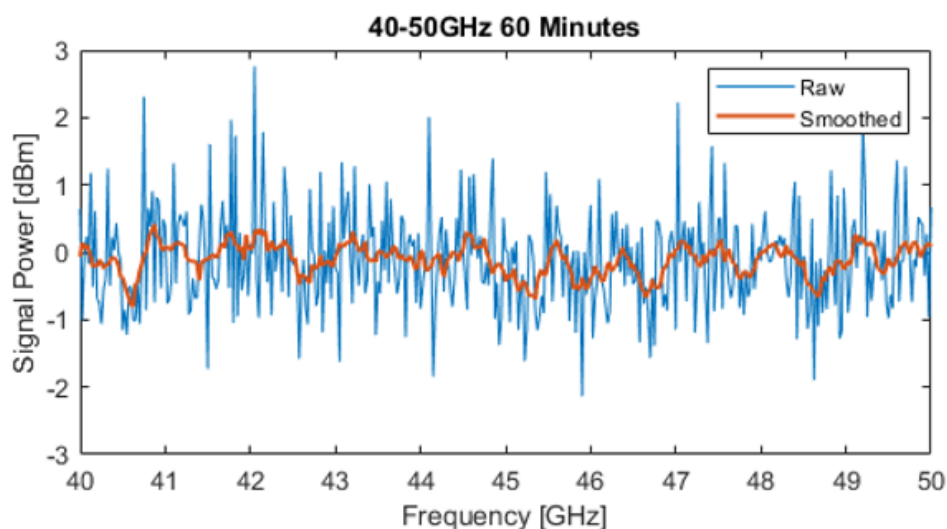
Figure 5.14: Example of the listening experiment results. Note that after smoothing, the signal power is exceptionally flat, never rising above 1 dBm. This is representative for all bandwidths and time instances measured.

5.5   Conclusions

Using frequency selective surfaces, we performed novel barrier experiments that allowed us to narrow down potential signal bandwidth with resolution far greater than previous experi-

ments. Experimental evidence suggests there is an effect in the receiver cells. Experiments over time suggest the effect is causal, suggesting it is a signal from the UV radiated cells. The distance experiments further suggest this by demonstrating the signal drops off at certain distance. Finally, the FSS experiments suggest the signal is frequency dependent, reinforcing that is EM in nature. This suggests the signal is in the range of 20 to 30 GHz.

Following this, we performed listening experiments to attempt to measure the signal directly. Low noise UWB amplifiers were used to probe the cells and detect extremely low power signals. We were unable to detect any signal whatsoever. Though not detailed in thesis, stimulation experiments were also performed in which signals in the range of 20-30 GHz were applied to cell cultures in the attempt to recreate the olive moment effect. Such experiments were also negative, providing no evidence of stimulation. Overall, the experimental evidence is conflicting.

This chapter uses material from "Evidence of intercellular electromagnetic communication in murine embryonic fibroblast culture" by BK Hsiung, KA Thackston, DF Sievenpiper, DD Deheyn. *In preparation*. All material is used with permission by the other authors. The dissertation author was the primary author of this material.

Chapter 6

Discussion

The hypothesis of electromagnetic signaling in biological systems has long been outside the mainstream of accepted science. The field has a long and controversial history, filled with irreproducible experiments, esoteric and convoluted hypotheses, and association with some of the more conspicuous characters of pseudo-science. When properly applied, however, the scientific method is agnostic to the question it is applied to. Objective study can still occur if we understand the limitations of the models used and carefully control our experiments.

This thesis has produced primarily negative results. Negative results still provide value by helping focus resources in broadly defined research subjects towards more productive directions. About 90 years ago, this is what happened with the original theory of EM signaling, mitogenetic radiation. Alexander Gurwitsch's studies in mitogenetic radiation in the 1920s and 30s produced controversy. The National Research council prioritized resolution of the subject. A well funded and rigorous attempt at replication produced negative results. Following communication of these results, research activity in the field ceased [7]. This is an example of a healthy and robust scientific community, one that allows theories to emerge from outside of the mainstream, but still subjects them to rigorous investigation and experiment. In this chapter, I will attempt to summarize the scope of our results and discuss which areas of research could be explored in the

future.

6.1 Conclusions of our Studies

6.1.1 Limitations on EM signaling with resonant biomolecules

The primary scope of our modeling involved the possibility that biomolecules with permanent charges or dipole moments could sustain high frequency mechanical vibration, and thus generate a high frequency EM field that could be used to signal a similar receiver. As other researchers such as Adair have pointed out previously, viscous damping by surrounding media is the biggest barrier to mechanical vibrations storing significant energy [54, 59]. Using a similar strategy, we began with an abstract model of a biological resonator and defined a minimum criterion on damping for EM signaling to occur.

In the far field, we found that biological resonators would have to be quite large to have a chance of absorbing significant electromagnetic energy from a low power (non thermal) plane wave. In the near field case, we found coupling had to be very strong between resonators to permit signaling, and even then it required Q factors larger than those previously identified in the literature. This analysis is not dependent on the electrical sensitivity of the resonator (i.e. how strong a dipole moment or how much charge is present). In order for vibrational resonances to result in viable signaling, it must be justified how viscous damping can be overcome.

6.1.2 Microtubules as EM Sources

Microtubules are the most commonly hypothesized biological antenna [68, 60, 40, 77]. This makes it the most obvious candidate for a study such as ours. In our study, we sought to bypass the question of *if* microtubules could sustain high frequency mechanical vibrations, and assume these vibrations exist and quantify their electrical activity.

We noticed in previous studies, the simulation method overestimated the range of the electric field and could only account for one type of vibration. We created our own simulation method which was more robust and could accommodate all vibrational types. This allowed us to identify that the flexing mode was in fact the most electrically active vibration, something that had not been previously identified in the literature. This was also the first study in which interactions between microtubules was quantified. We determined that microtubule vibrations would not generate strong enough fields to induce vibrations in neighboring microtubules. Microtubules are simply not electrically polar enough to overcome background thermal energy. It is possible, however, that the electric fields generated might be significant enough to interact with other proteins at distances beyond the Debye length. This could be of interest if these vibrations could be experimentally proven, but increasing interaction distance from a few angstroms to a few nanometers is hardly a biological antenna.

6.1.3 Electrodynamic Interaction Modeling

Our work simulating microtubules identified a gap in available molecular simulation techniques to handle electrodynamic interactions. Seeking to fill this gap, we borrowed from the theory of Cerenkov radiation in conductive media to model the counter-ion wake left behind by a moving charge [92, 91]. We extended this theory to a numerical model where the counter-ionic charge wake was represented with a discrete set of decaying charges. This agreed excellently with the macroscopic model of an oscillating dipole.

Having derived the relevant expressions, we sought to determine the regime where electro-dynamic interactions would be non-negligible in biological systems. Our analysis suggested the velocities required are high relative to typical ionic drift velocity. The electric fields required to drive such velocities would be much larger than one would expect for EM signaling. To confirm this, we implemented a rod bead model of linear DNA in a Brownian dynamics simulation. We indeed found that the DNA did not react until extremely large electric field stimulations were

applied.

While this virtual charge method is likely not necessary for simulations of weak EM fields, it could be applied to problems where relatively large field strengths are used, such as electroporation or tumor treating fields [87, 88, 102, 103]. Our computational method could be applied to situations where high velocities are achieved by mechanical means as well, such as motor proteins. This method of accounting for a counter-ion wake is not restricted to biological systems either, and could be applicable for simulations in plasma physics.

6.1.4   Experimental Results

Tangential from our modeling, we also conducted experiments to investigate EM signaling between cell cultures. To perform a more sophisticated version of barrier experiments, we developed our own frequency selective surfaces that acted as a series of bandpass filters, allowing us to narrow down the frequency range that EM signaling could occur at. The barrier experiments produced positive results, suggesting activity in the spectrum of $20\,\mathrm{GHz}$ to $30\,\mathrm{GHz}$. Subsequent RNAseq trials did not yet confirm any change in gene expression "receiver" cell cultures.

Listening experiments in the same frequency band were unable to detect any evidence of a biological signal. This could be because of insufficient gain or poor coupling between the cellular signal and our probe, or because of an absence of signal. Stimulation experiments in the same frequency band also did not result in any positive effect.

Overall the experiments were mixed in their findings. If another metric in addition to the olive moment assay could also demonstrate a positive effect, this would provide a much stronger case for the existence of signaling. This would also provide justification for more rigorous measurements. The measurement probe could certainly be optimized for better coupling to a biological signal. More analysis could also be spent on the minimum detectable limit of the system to guarantee we are indeed measuring sufficiently weak signals. Experimental work should guide direction of modeling. Without evidence of biological activity that cannot be explained

readily without EM signaling, many attempts at modeling will be shots in the dark.

6.2   Potential Future Work

6.2.1   Slip layers on charged surfaces

Many works maintain that microtubule vibrations would be able to overcome damping because of a "slip layer" at the charged surface [70, 72]. The idea is that the highly polar surface of the microtubule would repel ions and even water, creating a slip boundary condition at the surface of the microtubule, reducing viscous drag significantly. Others have also argued that water might be so polarized near the surface of the microtubule that it would become "ordered" and perhaps exhibit different viscous properties than typical water.

This slip layer has not been experimentally confirmed. Moreover, modern all-atom molecular dynamics simulations are seem sufficiently sophisticated to simulate and confirm or falsify the existence of such layers. It would be useful for future work either falsify the slip layer, or if confirmed, quantify the mechanical impact such a layer could have on biological resonances.

6.2.2   Collective resonance effects

Our work primarily focused on one or two resonators interacting. We did not take into account the effect of many weakly coupled resonators and how such collective action might alleviate the criterion for signaling. From our analysis, it does not seem likely to me collective action would make significant difference. As we saw in the case of the microtubules, the electric field drops off precipitously as a power of $1/r^4$. After moving just a few nanometers away, the field is no longer significant. A microtubule is already 23 nm in diameter; the "antenna" is therefore already larger than the range it operates at. Clearly there will be rapidly diminishing returns to packing many microtubules together.

This argument, however, is qualitative. A more rigorous study into the collective effect of biological resonators is warranted. There have been many previous attempts to model the effects of collective resonances in biological systems [104, 105, 106, 107, 108]. These works have been mostly theoretical physics studies, without much attempt to make them relevant to biology. Experimental works suggest that any collective action requires energy levels much greater than would be expected in EM signaling [21]. The "energy threshold" of such collective resonances remains an open question.

6.2.3 Radical Pair Mechanisms

In our work we only concerned ourselves with electro-mechanical coupling into bio-molecules. Another possible mechanism of detecting low power EM is by interfering with radical pair reactions. It has been shown that weak static magnetic fields (1 mT to 100 mT) can impact radical pair recombination [84]. These interactions could have various biological effects downstream, as has been demonstrated in photosynthesis or in the magnetosensing of birds [36].

Investigating this topic would likely require one to work at much smaller length scales than have been addressed in this thesis. This could involve quantum mechanics simulations that at the present are difficult to extend to the length scale of entire biomolecules.

Bibliography

[1] M. Cifra, J. Z. Fields, and A. Farhadi, "Electromagnetic cellular interactions," *Progress in Biophysics and Molecular Biology*, vol. 105, pp. 223–246, May 2011.

[2] J. Cover and M. Curd, *Philosophy of Science: The Central Issues*. W. W. Norton & Company, 1st ed., 1998.

[3] M. Blank and R. Goodman, "DNA is a fractal antenna in electromagnetic fields," *International Journal of Radiation Biology*, vol. 87, pp. 409–415, Apr. 2011. Publisher: Taylor & Francis _eprint: https://doi.org/10.3109/09553002.2011.538130.

[4] P. Singh, R. Doti, J. E. Lugo, J. Faubert, S. Rawat, S. Ghosh, K. Ray, and A. Bandyopadhyay, "DNA as an Electromagnetic Fractal Cavity Resonator: Its Universal Sensing and Fractal Antenna Behavior," in *Soft Computing: Theories and Applications* (M. Pant, K. Ray, T. K. Sharma, S. Rawat, and A. Bandyopadhyay, eds.), Advances in Intelligent Systems and Computing, (Singapore), pp. 213–223, Springer, 2018.

[5] D. Fels, "Electromagnetic cell communication and the barrier method," 2015.

[6] D. Fels, "Cellular Communication through Light," *PLOS ONE*, vol. 4, p. e5086, Apr. 2009.

[7] K. H. Stern, "Mitogenetic Radiation: A Study of Authority in Science," *Journal of the Washington Academy of Sciences*, vol. 65, no. 3, pp. 83–90, 1975.

[8] W. Metcalf and T. Quickenden, "Mitogenetic Radiation," *Nature Cytology*, vol. 216, pp. 169–170, Oct. 1967.

[9] "Langmuir's talk on Pathological Science."

[10] A. A. Gurwitsch, "A historical review of the problem of mitogenetic radiation," *Experientia*, vol. 44, pp. 545–550, July 1988.

[11] F.-A. Popp, Q. Gu, and K.-H. Li, "Biophoton emission: experimental background and theoretical approaches," *Modern Physics Letters B*, vol. 08, pp. 1269–1296, Sept. 1994. Publisher: World Scientific Publishing Co.

[12] R. V. Wijk and E. P. A. V. Wijk, "An Introduction to Human Biophoton Emission," *Complementary Medicine Research*, vol. 12, no. 2, pp. 77–83, 2005. Publisher: Karger Publishers.

[13] M. Cifra, C. Brouder, M. Nerudová, and O. Kučera, "Biophotons, coherence and photocount statistics: A critical review," *Journal of Luminescence*, vol. 164, pp. 38–51, Aug. 2015.

[14] "Biophoton therapy: an appraisal - IOCOB," June 2013.

[15] Y. Sun, C. Wang, and J. Dai, "Biophotons as neural communication signals demonstrated by in situ biophoton autography," *Photochemical & Photobiological Sciences*, vol. 9, no. 3, pp. 315–322, 2010. Publisher: Royal Society of Chemistry.

[16] "Biophoton Communication: Can Cells Talk Using Light?."

[17] H. Fröhlich, "Bose condensation of strongly excited longitudinal electric modes," *Physics Letters A*, vol. 26, pp. 402–403, Mar. 1968.

[18] H. Fröhlich, "Long-range coherence and energy storage in biological systems," *International Journal of Quantum Chemistry*, vol. 2, no. 5, pp. 641–649, 1968.

[19] H. Fröhlich, "Long Range Coherence and the Action of Enzymes," *Nature*, vol. 228, pp. 1093–1093, Dec. 1970.

[20] J. R. Reimers, L. K. McKemmish, R. H. McKenzie, A. E. Mark, and N. S. Hush, "Weak, strong, and coherent regimes of Fröhlich condensation and their applications to terahertz medicine and quantum consciousness," *Proceedings of the National Academy of Sciences*, vol. 106, pp. 4219–4224, Mar. 2009.

[21] I. V. Lundholm, H. Rodilla, W. Y. Wahlgren, A. Duelli, G. Bourenkov, J. Vukusic, R. Friedman, J. Stake, T. Schneider, and G. Katona, "Terahertz radiation induces non-thermal structural changes associated with Fröhlich condensation in a protein crystal," *Structural Dynamics*, vol. 2, p. 054702, Sept. 2015. Publisher: American Institute of Physics.

[22] "Collective Vibration In A Protein Crystal."

[23] I. N. Marshall, "Consciousness and Bose-Einstein condensates," *New Ideas in Psychology*, vol. 7, pp. 73–83, Jan. 1989.

[24] a. R. Vasconcellos, F. S. Vannucchi, S. Mascarenhas, and R. Luzzi, "Frohlich Condensate: Emergence of Synergetic Dissipative Structures in Information Processing Biological and Condensed Matter Systems," *Information; Basel*, vol. 3, no. 4, pp. 601–620, 2012. Num Pages: 601-620 Place: Basel, Switzerland, Basel Publisher: MDPI AG.

[25] R. Penrose, *The Emperor's New Mind: Concerning Computers, Minds, and the Laws of Physics*. Oxford University Press, 1989.

[26] A. Akhmanova and M. O. Steinmetz, "Control of microtubule organization and dynamics: two ends in the limelight," *Nature Reviews Molecular Cell Biology*, vol. 16, pp. 711–726, Dec. 2015.

[27] S. Hameroff and R. Penrose, "Consciousness in the universe: A review of the 'Orch OR' theory," *Physics of Life Reviews*, vol. 11, pp. 39–78, Mar. 2014.

[28] S. M. Hameroff, "How quantum brain biology can rescue conscious free will," *Frontiers in Integrative Neuroscience*, vol. 6, 2012. Publisher: Frontiers.

[29] J. R. Reimers, L. K. McKemmish, R. H. McKenzie, A. E. Mark, and N. S. Hush, "The revised Penrose–Hameroff orchestrated objective-reduction proposal for human consciousness is not scientifically justified: Comment on "Consciousness in the universe: A review of the 'Orch OR' theory" by Hameroff and Penrose," *Physics of Life Reviews*, vol. 11, pp. 101–103, Mar. 2014.

[30] B. J. Baars and D. B. Edelman, "Consciousness, biology and quantum hypotheses," *Physics of Life Reviews*, vol. 9, pp. 285–294, Sept. 2012.

[31] "On the quantum theory of consciousness," June 2015.

[32] M. Tegmark, "Importance of quantum decoherence in brain processes," *Physical Review E*, vol. 61, pp. 4194–4206, Apr. 2000. Publisher: American Physical Society.

[33] H. Putnam, "Book Review of Shadow of the Mind," *Bulletins of the American Mathematical Society*, vol. 32, pp. 370–373, 1995.

[34] L. K. McKemmish, J. R. Reimers, R. H. McKenzie, A. E. Mark, and N. S. Hush, "Penrose-Hameroff orchestrated objective-reduction proposal for human consciousness is not biologically feasible," *Physical Review E*, vol. 80, p. 021912, Aug. 2009. Publisher: American Physical Society.

[35] "FCC Policy on Human Exposure," Nov. 2015.

[36] C. Nießner, S. Denzau, K. Stapput, M. Ahmad, L. Peichl, W. Wiltschko, and R. Wiltschko, "Magnetoreception: activated cryptochrome 1a concurs with magnetic orientation in birds," *Journal of The Royal Society Interface*, vol. 10, p. 20130638, Nov. 2013. Publisher: Royal Society.

[37] M. G. Paulin, "Electroreception and the compass sense of sharks," *Journal of Theoretical Biology*, vol. 174, pp. 325–339, June 1995.

[38] P. Moller, "'Communication' in weakly electric fish, Gnathonemus niger (Mormyridae) I. Variation of electric organ discharge (EOD) frequency elicited by controlled electric stimuli," *Animal Behaviour*, vol. 18, pp. 768–786, Nov. 1970.

[39] D. Clarke, H. Whitney, G. Sutton, and D. Robert, "Detection and Learning of Floral Electric Fields by Bumblebees," *Science*, vol. 340, pp. 66–69, Apr. 2013. Publisher: American Association for the Advancement of Science Section: Report.

[40] M. Cifra, J. Pokorný, D. Havelka, and O. Kučera, "Electric field generated by axial longitudinal vibration modes of microtubule," *Biosystems*, vol. 100, pp. 122–131, May 2010.

[41] O. Kučera, D. Havelka, and M. Cifra, "Vibrations of microtubules: Physics that has not met biology yet," *Wave Motion*, vol. 72, pp. 13–22, July 2017.

[42] K. A. Thackston, D. D. Deheyn, and D. F. Sievenpiper, "Simulation of electric fields generated from microtubule vibrations," *Physical Review E*, vol. 100, p. 022410, Aug. 2019.

[43] P. V. Zinin, J. S. Allen, and V. M. Levin, "Mechanical resonances of bacteria cells," *Physical Review E*, vol. 72, Dec. 2005.

[44] T.-M. Liu, H.-P. Chen, S.-C. Yeh, C.-Y. Wu, C.-H. Wang, T.-N. Luo, Y.-J. Chen, S.-I. Liu, and C.-K. Sun, "Effects of hydration levels on the bandwidth of microwave resonant absorption induced by confined acoustic vibrations," *Applied Physics Letters*, vol. 95, p. 173702, Oct. 2009.

[45] T.-M. Liu, H.-P. Chen, L.-T. Wang, J.-R. Wang, T.-N. Luo, Y.-J. Chen, S.-I. Liu, and C.-K. Sun, "Microwave resonant absorption of viruses through dipolar coupling with confined acoustic vibrations," *Applied Physics Letters*, vol. 94, p. 043902, Jan. 2009.

[46] S.-C. Yang, H.-C. Lin, T.-M. Liu, J.-T. Lu, W.-T. Hung, Y.-R. Huang, Y.-C. Tsai, C.-L. Kao, S.-Y. Chen, and C.-K. Sun, "Efficient Structure Resonance Energy Transfer from Microwaves to Confined Acoustic Vibrations in Viruses," *Scientific Reports*, vol. 5, pp. 1–10, Dec. 2015.

[47] C.-K. Sun, Y.-C. Tsai, Y.-J. E. Chen, T.-M. Liu, H.-Y. Chen, H.-C. Wang, and C.-F. Lo, "Resonant Dipolar Coupling of Microwaves with Confined Acoustic Vibrations in a Rod-shaped Virus," *Scientific Reports*, vol. 7, pp. 1–9, July 2017.

[48] G. S. Edwards, C. C. Davis, J. D. Saffer, and M. L. Swicord, "Resonant Microwave Absorption of Selected DNA Molecules," *Physical Review Letters*, vol. 53, pp. 1284–1287, Sept. 1984.

[49] L. L. Van Zandt, "Resonant Microwave Absorption by Dissolved DNA," *Physical Review Letters*, vol. 57, pp. 2085–2087, Oct. 1986.

[50] M. Cifra, "Electrodynamic eigenmodes in cellular morphology," *Biosystems*, vol. 109, pp. 356–366, Sept. 2012.

[51] R. Phillips, J. Kondev, J. Theriot, and H. Garcia, "Electrostatics for Salty Solutions," in *Physical Biology of the Cell*, Garland Science, 2 ed., 2013.

[52] J. R. de Xammar Oro, G. Ruderman, and J. R. Grigera, "Electrodynamics of interactions in electrolyte media. Possible consequences in biological functions," *Biophysics*, vol. 53, pp. 195–198, June 2008.

[53] J. Grigera, F. Vericat, G. Ruderman, and J. R. De Xammar Oro, "On the threshold frequency of long-range interactions in physiological solutions," *Chemical Physics Letters*, vol. 156, pp. 615–618, Apr. 1989.

[54] R. K. Adair, "Vibrational Resonances in Biological Systems at Microwave Frequencies," *Biophysical Journal*, vol. 82, pp. 1147–1152, Mar. 2002.

[55] R. E. Hamam, A. Karalis, J. D. Joannopoulos, and M. Soljačić, "Coupled-mode theory for general free-space resonant scattering of waves," *Physical Review A*, vol. 75, p. 053801, May 2007.

[56] J. Jackson, *Classical Electrodynamics*. New York: Wiley.

[57] H. A. Wheeler, "Fundamental Limitations of Small Antennas," *Proceedings of the IRE*, vol. 35, pp. 1479–1484, Dec. 1947.

[58] R. Milo, R. Phillips, and N. Orme, *Cell Biology by the Numbers*. Garland Science, 2016.

[59] R. K. Adair, "Biophysical limits on athermal effects of RF and microwave radiation," *Bioelectromagnetics*, vol. 24, pp. 39–48, Jan. 2003.

[60] D. Havelka, M. Cifra, O. Kučera, J. Pokorný, and J. Vrba, "High-frequency electric field and radiation characteristics of cellular microtubule network," *Journal of Theoretical Biology*, vol. 286, pp. 31–40, Oct. 2011.

[61] J.-S. Hong, *Microstrip Filters for RF/Microwave Applications*. Wiley Series in Microwave and Optical Engineering, John Wiley & Sons, Inc, 2nd ed., 2011.

[62] D. Newland, "Calculation of Power Flow Between Coupled Oscillators," *Journal of Sound Vibration*, vol. 3, no. 3, pp. 262–276, 1966.

[63] J. A. Tuszyński, J. A. Brown, E. Crawford, E. J. Carpenter, M. L. A. Nip, J. M. Dixon, and M. V. Satarić, "Molecular dynamics simulations of tubulin structure and calculations of electrostatic properties of microtubules," *Mathematical and Computer Modelling*, vol. 41, pp. 1055–1070, May 2005.

[64] M. A. Deriu, M. Soncini, M. Orsi, M. Patel, J. W. Essex, F. M. Montevecchi, and A. Redaelli, "Anisotropic Elastic Network Modeling of Entire Microtubules," *Biophysical Journal*, vol. 99, pp. 2190–2199, Oct. 2010.

[65] K. A. Thackston, H. Mei, and P. P. Irazoqui, "Coupling Matrix Synthesis and Impedance-Matching Optimization Method for Magnetic Resonance Coupling Systems," *IEEE Transactions on Microwave Theory and Techniques*, vol. 66, pp. 1536–1542, Mar. 2018.

[66] D. M. Kesler, "Highly Resonant Wireless Power Transfer: Safe, Efficient, and over Distance," tech. rep., WiTricity Corporation, 2017.

[67] A. Samarbakhsh and J. A. Tuszynski, "Vibrational dynamics of bio- and nano-filaments in viscous solution subjected to ultrasound: implications for microtubules," *European Biophysics Journal*, vol. 40, pp. 937–946, Aug. 2011.

[68] D. Havelka, O. Kučera, M. A. Deriu, and M. Cifra, "Electro-Acoustic Behavior of the Mitotic Spindle: A Semi-Classical Coarse-Grained Model," *PLoS ONE*, vol. 9, p. e86501, Jan. 2014.

[69] K. R. Foster and J. W. Baish, "Viscous Damping of Vibrations in Microtubules," *Journal of Biological Physics*, vol. 26, pp. 255–260, Dec. 2000.

[70] J. Pokorný, "Viscous Effects on Polar Vibrations in Microtubules," *Electromagnetic Biology and Medicine*, vol. 22, pp. 15–29, Jan. 2003.

[71] O. Krivosudský and M. Cifra, "Microwave absorption by nanoresonator vibrations tuned with surface modification," *EPL (Europhysics Letters)*, vol. 115, p. 44003, Aug. 2016. Publisher: IOP Publishing.

[72] S. Li, C. Wang, and P. Nithiarasu, "Simulations on an undamped electromechanical vibration of microtubules in cytosol," *Applied Physics Letters*, vol. 114, p. 253702, June 2019.

[73] Y. Zhao and Q. Zhan, "Electric fields generated by synchronized oscillations of microtubules, centrosomes and chromosomes regulate the dynamics of mitosis and meiosis," *Theoretical Biology and Medical Modelling*, vol. 9, p. 26, July 2012.

[74] A. D. Ninno and M. Pregnolato, "Electromagnetic homeostasis and the role of low-amplitude electromagnetic fields on life organization," *Electromagnetic Biology and Medicine*, vol. 36, pp. 115–122, Apr. 2017.

[75] J. Pokorný, "Physical aspects of biological activity and cancer," *AIP Advances*, vol. 2, p. 011207, Mar. 2012.

[76] J. Pokorný, F. Jelínek, V. Trkal, I. Lamprecht, and R. Hölzel, "Vibrations in Microtubules," *Journal of Biological Physics*, vol. 23, pp. 171–179, Sept. 1997.

[77] J. Pokorny, F. Jelinek, and V. Trkal, "Electric field around microtubules," *Bioelectrochemistry and Bioenergetics*, vol. 45, pp. 239–245, May 1998.

[78] O. Kučera and D. Havelka, "Mechano-electrical vibrations of microtubules—Link to subcellular morphology," *Biosystems*, vol. 109, pp. 346–355, Sept. 2012.

[79] L. A. Amos, "The microtubule lattice — 20 years on," *Trends in Cell Biology*, vol. 5, pp. 48–51, Feb. 1995.

[80] D. Havelka, M. A. Deriu, M. Cifra, and O. Kučera, "Deformation pattern in vibrating microtubule: Structural mechanics study based on an atomistic approach," *Scientific Reports*, vol. 7, Dec. 2017.

[81] H. Myers, *Introductory Solid State Phyics*. Taylor and Francis, second ed., 1997.

[82] D. J. Griffiths, *Introduction to Electrodynamics*. Prentice-Hall, 1 ed., 1981.

[83] C. E. Felder, J. Prilusky, I. Silman, and J. L. Sussman, "A server and database for dipole moments of proteins," *Nucleic Acids Research*, vol. 35, pp. W512–W521, July 2007.

[84] F. Apollonio, M. Liberti, A. Paffi, C. Merla, P. Marracino, A. Denzi, C. Marino, and G. d'Inzeo, "Feasibility for Microwaves Energy to Affect Biological Systems Via Nonthermal Mechanisms: A Systematic Approach," *IEEE Transactions on Microwave Theory and Techniques*, vol. 61, pp. 2031–2045, May 2013.

[85] M. Ozboyaci, D. B. Kokh, S. Corni, and R. C. Wade, "Modeling and simulation of protein–surface interactions: achievements and challenges," *Quarterly Reviews of Biophysics*, vol. 49, p. e4, 2016.

[86] A. Satoh, *Introduction to Practice of Molecular Simulation*. Elsevier, 2011.

[87] C. Wenger, P. C. Miranda, R. Salvador, A. Thielscher, Z. Bomzon, M. Giladi, M. M. Mrugala, and A. R. Korshoej, "A Review on Tumor-Treating Fields (TTFields): Clinical Implications Inferred From Computational Modeling," *IEEE Reviews in Biomedical Engineering*, vol. 11, pp. 195–207, 2018.

[88] W. Krassowska and P. D. Filev, "Modeling Electroporation in a Single Cell," *Biophysical Journal*, vol. 92, pp. 404–417, Jan. 2007.

[89] C. Tai, "A study of electrodynamics of moving media," *Proceedings of the IEEE*, vol. 52, pp. 685–689, June 1964.

[90] C. Tai, V. Pyati, and R. Kalafus, "Topics in Electrodynamics of Moving Media," Grant Update 7322-1-F, University of Michigan, NASA, 1966.

[91] R. M. Kalafus, "Radiation from sources in a moving, conducting medium," *Radio Science*, vol. 4, pp. 977–982, Oct. 1969.

[92] R. Kalafus, *Electromagnetism in Moving, Conductive Media*. Doctoral Dissertation, University of Michigan, 1968.

[93] C. T. Tai and R. E. Collin, "Radiation of a Hertzian dipole immersed in a dissipative medium," *IEEE Transactions on Antennas and Propagation*, vol. 48, pp. 1501–1506, Oct. 2000.

[94] J. Langowski, "Polymer chain models of DNA and chromatin," *The European Physical Journal E*, vol. 19, pp. 241–249, Mar. 2006.

[95] A. K. Mazur, "Wormlike Chain Theory and Bending of Short DNA," *Physical Review Letters*, vol. 98, p. 218102, May 2007. Publisher: American Physical Society.

[96] H. Jian, A. V. Vologodskii, and T. Schlick, "A Combined Wormlike-Chain and Bead Model for Dynamic Simulations of Long Linear DNA," *Journal of Computational Physics*, vol. 136, pp. 168–179, Sept. 1997.

[97] S. A. Allison, "Brownian dynamics simulation of wormlike chains. Fluorescence depolarization and depolarized light scattering," *Macromolecules*, vol. 19, pp. 118–124, Jan. 1986.

[98] D. L. Ermak and J. A. McCammon, "Brownian dynamics with hydrodynamic interactions," *The Journal of Chemical Physics*, vol. 69, pp. 1352–1360, Aug. 1978. Publisher: American Institute of Physics.

[99] O. Kučera, M. Cifra, and J. Pokorný, "Technical aspects of measurement of cellular electromagnetic activity," *European Biophysics Journal*, vol. 39, pp. 1465–1470, Sept. 2010.

[100] B. Munk, *Frequency Selective Surfaces: Theory and Design*. Wiley, 1st ed., 2000.

[101] S. M. A. M. H. Abadi, M. Li, and N. Behdad, "Harmonic-Suppressed Miniaturized-Element Frequency Selective Surfaces With Higher Order Bandpass Responses," *IEEE Transactions on Antennas and Propagation*, vol. 62, pp. 2562–2571, May 2014. Conference Name: IEEE Transactions on Antennas and Propagation.

[102] M. Tarek, "Membrane Electroporation: A Molecular Dynamics Simulation," *Biophysical Journal*, vol. 88, pp. 4045–4053, June 2005.

[103] E. Goldberg, C. Suárez, M. Alfonso, J. Marchese, A. Soba, and G. Marshall, "Cell membrane electroporation modeling: A multiphysics approach," *Bioelectrochemistry*, vol. 124, pp. 28–39, Dec. 2018.

[104] J. Preto, "Classical investigation of long-range coherence in biological systems," *Chaos: An Interdisciplinary Journal of Nonlinear Science*, vol. 26, p. 123116, Dec. 2016. Publisher: American Institute of Physics.

[105] J. Preto, M. Pettini, and J. A. Tuszynski, "Possible role of electrodynamic interactions in long-distance biomolecular recognition," *Physical Review E*, vol. 91, p. 052710, May 2015. Publisher: American Physical Society.

[106] I. Nardecchia, L. Spinelli, J. Preto, M. Gori, E. Floriani, S. Jaeger, P. Ferrier, and M. Pettini, "Experimental detection of long-distance interactions between biomolecules through their diffusion behavior: Numerical study," *Physical Review E*, vol. 90, p. 022703, Aug. 2014.

[107] I. Nardecchia, J. Torres, M. Lechelon, V. Giliberti, M. Ortolani, P. Nouvel, M. Gori, Y. Meriguet, I. Donato, J. Preto, L. Varani, J. Sturgis, and M. Pettini, "Out-of-Equilibrium Collective Oscillation as Phonon Condensation in a Model Protein," *Physical Review X*, vol. 8, p. 031061, Sept. 2018.

[108] S. Olmi, M. Gori, I. Donato, and M. Pettini, "Collective behavior of oscillating electric dipoles," *Scientific Reports*, vol. 8, p. 15748, Oct. 2018. Number: 1 Publisher: Nature Publishing Group.